Journal of Volcanology and Geothermal Research 420 (2021) 107390

Contents lists available at ScienceDirect

Journal of Volcanology and Geothermal Research

journal homepage: www.elsevier.com/locate/jvolgeores

Zircon as a tracer of plumbing processes in an active magmatic system: insights from mingled magmas of the 2010 dome collapse, Montserrat, Lesser Antilles Arc, Caribbean

Jane H. Scarrow [a,b,*], Axel K. Schmitt [c], Jenni Barclay [b], Matthew S.A. Horstwood [d], Andrew J. Bloore [b], Thomas E. Christopher [e,f]

[a] Department of Mineralogy and Petrology, University of Granada, Campus Fuentenueva, Granada 18002, Spain
[b] School of Environmental Sciences, University of East Anglia, Norwich NR4 7TJ, UK
[c] Universität Heidelberg, Institut für Geowissenschaften, Im Neuenheimer Feld 234-236, Germany
[d] British Geological Survey, Keyworth, Nottingham NG12 5GG, UK
[e] Montserrat Volcano Observatory, Hope Drive, Flemmings, Montserrat
[f] The University of the West Indies Seismic Research Centre, Gordon St, Trinidad and Tobago

ARTICLE INFO

Article history:
Received 8 November 2020
Received in revised form 18 July 2021
Accepted 5 September 2021
Available online xxxx

Keywords:
Transcrustal magma reservoirs
Mafic enclaves
^{238}U-^{230}Th ages
Hf isotopes
Trace elements

ABSTRACT

Soufrière Hills Volcano, Montserrat, erupted from 1995 to 2010, with activity including dome growth, destructive pyroclastic density currents and Vulcanian explosions. Monitoring data, such as gas emissions, show the system is still in a state of unrest. The recent eruptions provide an opportunity to study, in real time, a complex subduction-related subvolcanic transcrustal melt-mush reservoir, its magma fluxes, and the timing of crystal and melt storage prior to eruptive paroxysms. How and when mush destabilisation occurs prior to volcanic eruptions continues to be a question of intense debate. Evidence of mafic magma intrusion, a potential eruptive trigger, is preserved in enclaves with quenched and diffuse margins that are mingled with crystal-rich andesite. Here, in this first study of Soufrière Hills Volcano zircon, we report zircon ages and compositions for mafic-intermediate enclaves and host andesites from the most recent dome collapse in 2010 to place temporal constraints on magma reservoir processes. Zircon ^{238}U-^{230}Th disequilibrium crystallisation ages ranging between c. 2–250 ka constrain the longevity of the magmatic plumbing system. Uniform Hf isotopes, εHf 11.3 ± 1.2 to 14.6 ± 1.5, indicate invariant compositions that are typical for island arc magma sources. Zircon trace element concentrations and Ti-in-zircon crystallisation temperatures indicate crystallisation in isolated, small-volume, lenses with variable fractions of melt of heterogeneous compositions. We suggest amalgamation of assorted crystal cargoes from these lenses occurred prior to eruption during mush destabilisation triggered by mafic magma recharge. Zircon textures, on the other hand, shed light on recent centimetre-scale magma mingling immediately prior to eruption. Euhedral-subhedral zircon is preferentially preserved in or near quenched contacts of the least-evolved enclave and host andesite. By contrast, reheating of the andesite by the mafic magma recharge in the presence of zircon-undersaturated melts promoted zircon resorption. This led to the formation of subhedral-anhedral corroded zircon that is typical in the host andesite mush. Zircon thus reveals processes ranging from 100,000s of years of andesite storage to short-term partial destruction in response to transient heating and magma mixing events.

1. Introduction

Characterisation of magmatic processes is critical to the understanding of long-term dynamics of volcanic activity. Soufrière Hills Volcano (SHV), a stratovolcano on the Caribbean island of Montserrat (Fig. 1), is an active geological hazard, it is unknown whether recent volcanic activity has now ceased or may reinitiate. The only historical eruption of SHV began in 1995 after c. 350 years of quiescence (Young et al., 1998) and continued to 2010 in five discrete episodes, phases I–V

* Corresponding author at: Department of Mineralogy and Petrology, University of Granada, Campus Fuentenueva, Granada 18002, Spain.
E-mail addresses: jscarrow@ugr.es (J.H. Scarrow), axel.schmitt@geow.uni-heidelberg.de (A.K. Schmitt), j.barclay@uea.ac.uk (J. Barclay), msah@bgs.ac.uk (M.S.A. Horstwood), thomas@mvo.ms (T.E. Christopher).

https://doi.org/10.1016/j.jvolgeores.2021.107390

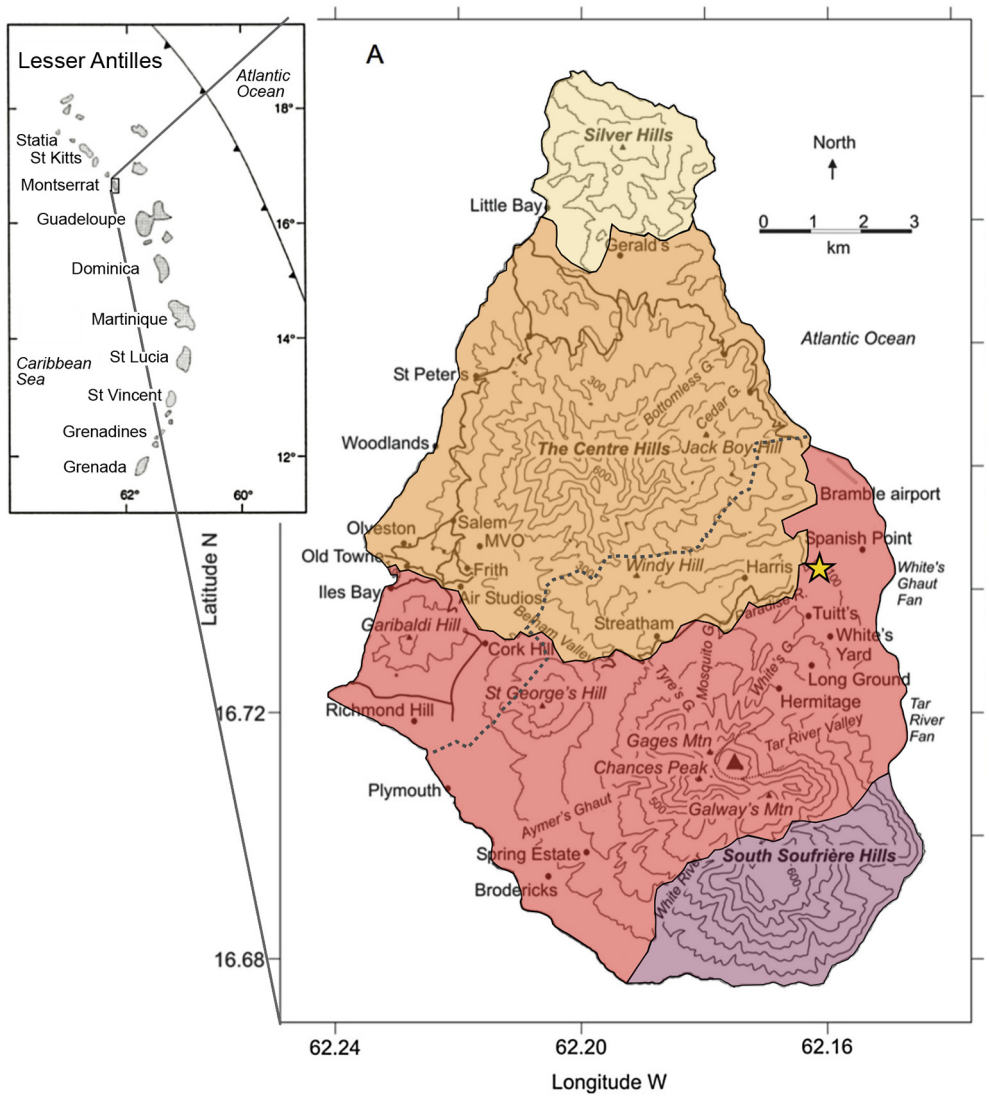

Fig. 1. Map of Montserrat, showing the Soufrière Hills Volcano, South Soufrière Hills, Centre Hills and Silver Hills (after Plail et al., 2018). Inset: map of the Lesser Antilles island arc. The current limit of the area with controlled access is marked with a dashed line. The sampling location is marked with a star. From north to south: Silver Hills – pale yellow (c. 2170–1030 ka); Centre Hills – pale orange (c. 1140–380 ka); Soufrière Hills – pale red (450 ka–present); South Soufrière Hills – pale purple (c. 130 ka). Ages from Hatter et al. (2018). (For interpretation of the references to colour in this figure legend, the reader is referred to the web version of this article.)

(Wadge et al., 2014 and references therein). The longevity and variability of the eruption makes it particularly suited to the study of magmatic processes and eruptive triggers. The recent SHV eruptions have included passive dome growth, destructive pyroclastic density currents, including a lateral blast, and Vulcanian explosions (Fig. 2a and b). Pre-existing petrological work provides excellent constraints on magmatic intensive variables and their variance as well as a framework of models into which new data and findings can be integrated (e.g., Murphy et al., 2000; Zellmer et al., 2003a; Christopher et al., 2014; Plail et al., 2018). Comprehensive quantitative observations of surface activity and geophysical constraints on subsurface changes are available in an exceptional monitoring dataset, these can place important independent controls on petrological models (cf., Kahl et al., 2013; Pankhurst et al., 2018).

Early in the SHV eruption the underlying driving forces for its activity were interpreted to be recharge of mafic magma remobilising an 'andesitic mush', by addition of heat and volatiles (Murphy et al., 2000; Sparks and Young, 2002). As the volcanic activity progressed, additional ideas about magma interactions were developed and long-term monitoring and rock record data pointed to continued recharge and complex magma storage and plumbing (Wadge et al., 2014 and references therein). Mafic magma remnants are ubiquitously preserved as mingled mafic-intermediate enclaves (henceforth referred to as enclaves) in host andesites. These enclaves show textures including quenched, crenulated and diffuse margins which collectively indicate that mafic magma was entrained in the andesite (Fig. 2c and d). Recently, however, various lines of evidence are converging to suggest that mafic magma recharge ceased prior to the most recent activity. For example, a five-fold increase in enclave abundance and the appearance of porphyritic enclaves during phase III, i.e., mid-2005 to early-2007, of the activity led Barclay et al. (2010) to suggest that interaction between andesite and mafic recharge could have occurred during the course of that eruptive phase. More generally, Plail et al. (2018) interpreted changes from phase I to V of activity to indicate the cessation of mafic magma recharge after phase III. They attributed an increase in enclave size and abundance, in particular of mingled enclaves, to resultant thickening of a hybrid layer at the mafic magma-andesite interface. Furthermore, Nd isotope ratio variations show that andesite magma and enclave interaction peaked during phase III (Cassidy et al., 2012), whereas whole-rock Pb isotope data indicate the composition of

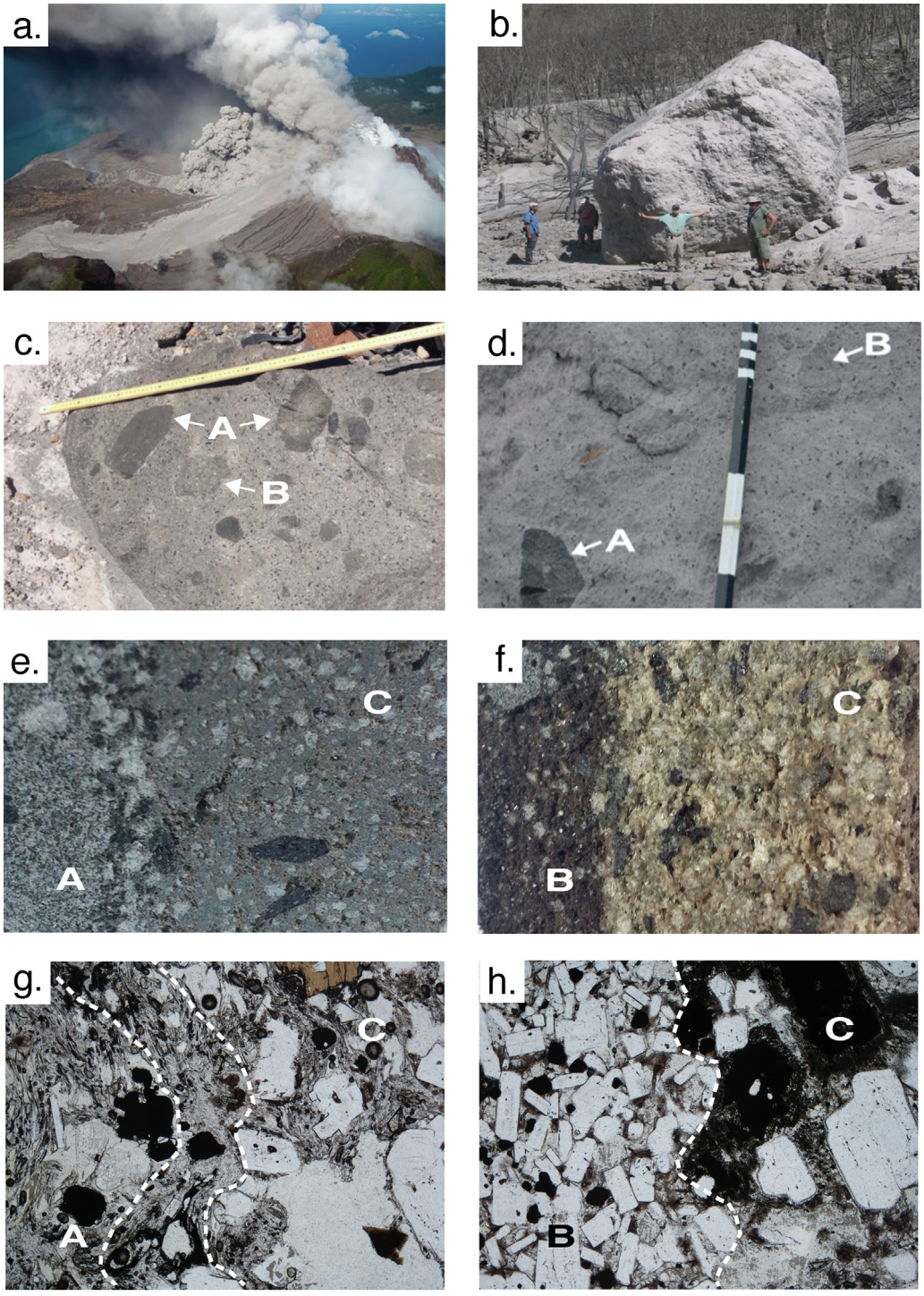

Fig. 2. a. Pyroclastic density current from a dome collapse to the southwest of Soufrière Hills Volcano, near Brodericks, November 2009 (from Wadge et al., 2014); b. Large block of dome lava in the dome-collapse pyroclastic density current deposits, February 2010, to the northeast of Soufrière Hills Volcano, near Harris (from Wadge et al., 2014); c. Field photograph of enclaves in a block of andesite, A: type A enclave with a quenched contact, B: type B enclave with a diffuse contact, tape measure 90 cm (from Plail et al., 2014); d. Field photograph of enclaves in a block of andesite, A: type A enclave with a quenched contact, B: type B enclave with a diffuse contact, scale 30 cm (from Plail et al., 2014); e. Hand specimen close up of the quenched contact between the enclave, left-hand side, and andesite, right-hand side, in the least-evolved sample JHS-3, width of field of view 3 cm. A: type A enclave with a quenched contact, C: andesite; f. Hand specimen close up of the diffuse contact between the enclave, left-hand side, and andesite, right-hand side, in the most-evolved sample JHS-7, width of field of view 3 cm. B: type B enclave with a diffuse contact, C: andesite; g. Photomicrograph of the contact between an enclave, left, and crystal-rich andesite, right, with glassy matrix at the contact between the two, width of field of view 0.7 cm. Quenched glassy contact marked with dashed white lines; h. Photomicrograph of an enclave with diktytaxitic texture, left, formed of white tabular plagioclase and subhedral brown amphibole, with pale interstitial glass and crystal-rich andesite right, width of field of view 0.7 cm. Contact marked with dashed white line. (For interpretation of the references to colour in this figure legend, the reader is referred to the web version of this article.)

magma sources – including sediment and slab fluid inputs – remained fairly constant during the most recent activity. In addition, a study of whole-rock U-series disequilibria in enclaves and host andesite by McGee et al. (2019) suggested that the magmatic system was closed to fresh gas influx from phase III onwards, which implies that the influx of mafic magma had ceased and current SO_2 emissions could quite likely

be related to residual degassing. Their modelling suggested sporadic enclave entrainment into the andesite prior to eruption, but critically, did not suggest mafic magma influx as a trigger for each eruptive phase. Likewise, Sheldrake et al. (2020) studying aragonite coral skeleton compositions as tracers of water column chemistry, noted a tailing off of Mg/Ca spikes – related to the presence of relatively Mg-rich volcanic ash in the marine environment – after phase III. What is more, recent modelling of the regional ground deformation, continuing regional uplift, of the island has been interpreted as viscoelastic rebound resulting from removal of a significant mass of sub-volcanic magma early in the activity rather than continued magma recharge (Neuberg and Pascal, 2020). Considering these new findings, we propose that careful study of mineral phase ages, compositions, proportions and textures is an effective way to identify and unpick, even cryptic, magma mixing processes (cf. Ubide and Kamber, 2018; Cisneros de León and Schmitt, 2019).

Although SHV is one of the most studied volcanoes in the world, to date zircon – a unique tool for deciphering magma storage duration and conditions – has not been characterised in the SHV enclaves and intermediate andesite host magma components. Notably, SHV is the type locality for development of the paradigm-shifting magma reservoir model of transcrustal mush in which melt-rich layers destabilise, ascend, and accumulate in shallow transient chambers (Christopher et al., 2015; Cashman et al., 2017). The model predicts that mush destabilisation can explain the presence of minerals with very different histories in the same erupted rock sample, for example, amalgamation of zircon grains crystallised tens or hundreds of thousands of years prior to eruption (cf., Miller and Wooden, 2004; Claiborne et al., 2010; Storm et al., 2012a; Howe et al., 2015). Where and for how long minerals and melts are stored and how these factors influence eruptive potential are important questions about magma reservoir processes (Cooper, 2019). Are crystal cargoes in erupted magmas long-lived records of a 'cool' mush that was entrained into 'warm' melt just before eruption, and if so how and why did mush destabilisation occur? Such information can be fed into models of volcanic risk at island arcs, in particular related to medium-long term hazard mitigation planning strategies.

Here we report zircon ages and compositions for SHV enclaves and host andesites from the 2010 dome collapse combining fieldwork, petrography, mineral chemistry, whole-rock geochemistry, zircon U-series geochronology and mineral chemistry Hf isotopes and trace-element abundances including Ti and rare earth elements. These data add an additional perspective that permits us to shed light on reconstruction of the dynamic magma storage architecture over tens of thousands of years and constrain timescales of magma mingling which occurred within decadal timescales of eruptive activity.

2. Geological background and field relations

Montserrat is located in the northern Lesser Antilles arc which has been active for c. 40 Ma as a result of westward subduction of the North American plate under the Caribbean plate (Bouysse and Westercamp, 1990). The island has three main volcanic centres (Fig. 1) (Harford et al., 2002; Coussens et al., 2017; Hatter et al., 2018). In the north, Silver Hills activity (c. 2170–1030 ka) comprised periodic andesite lava dome growth and collapse resulting in volcaniclastic sequences, explosive Vulcanian style eruptions, and sector collapse events with related debris avalanche deposits. Centre Hills (c. 1140–380 ka), in the middle of the island, was the most explosive centre. It produced block-and-ash flows, pumice-and-ash flows, pumice falls, lahars, and debris avalanche deposits. To the south, South Soufrière (c. 130 ka), part of the SHV, erupted basalt and basaltic andesite lava flows, scoria-fall deposits and minor andesites. The SHV (450 ka-present) has been dominated by effusive dome growth, associated collapse-related pyroclastic density currents, and pumice fall from Vulcanian explosions.

The most recent SHV eruptive activity between 1995 and 2010 began after over 350 years of relative quiescence (Young et al., 1998). The eruptions followed detection of seismic swarms when equipment was reinstalled in 1992 after Hurricane Hugo destroyed the monitoring network in 1989 (Murphy et al., 2000). Unusually, activity has lasted for 15 years, with the next longest event known in the region being Mont Pelée, Martinique which erupted for only 3.5 years from 1902 to 1905. The recent SHV activity is divided into five phases separated by residual activity without lava extrusion. Phase I, late-1995 to early-1998, began with phreatic activity and comprised cycles of andesite dome extrusion, dome collapse-related pyroclastic density currents and Vulcanian explosions (Wadge et al., 2014). Phase II, late-1999 to mid-2003, and Phase III, mid-2005 to early-2007, were dominated by dome growth and collapse (Christopher et al., 2014). Phase IV, mid-2008 to early-2009, was more explosive including Vulcanian activity in addition to dome growth and collapse events (Wadge et al., 2014). Finally Phase V, late-2009 to early-2010, was also explosive, with ash venting Vulcanian activity terminating with a dome collapse (Stinton et al., 2014). The southern half of the island continues to be an uninhabitable exclusion zone (Fig. 1).

3. Sample description

This study investigates enclaves and crystal-rich host andesites sampled in metre-scale block-and-ash flow outcrops of the terminal exogenous dome collapse in 2010 that revealed rocks from the interior of the endogenous dome, sub-volcanic magma reservoir, close to the crater (Fig. 2b). Enclave abundance has varied through the recent eruptions: increasing in volume from phase I, ~1%, to phase V, ~8–12%; and in apparent size, from ~2–3 cm to 5–6 cm in diameter in phase I, to <14 cm in phase III and up to ~25 cm in phase V (Barclay et al., 2010; Plail et al., 2018). Barclay et al. (2010) identified four types of enclaves in the field: i. diktytaxitic as defined by abundant interstitial cavities between plagioclase laths; ii. waxy; iii. mixed – with a distinct border with the andesite; and iv. undifferentiated. The least-evolved, basaltic, enclaves are phenocryst-poor whereas the more intermediate, basaltic-andesite, compositions are porphyritic. The enclave borders are mostly rounded but some have crenulated, wispy, pillow-shaped, or quenched margins.

We investigated if zircon was present in multiple thin sections of more than 20 different samples of andesite and enclaves from the most recent eruptive phase V using an optical cathodoluminescence microscope. This permitted identification of crystals not clearly visible in plane polarised light or under cross polars. Some thin sections were just of andesite, others just of enclave whereas many captured both andesite and enclave and the contact between them. In the enclaves, zircon was only rarely present, generally as a single isolated grain. In the andesite samples, zircon was also scarce, typically one to three grains per thin section most commonly present as inclusions in amphibole phenocrysts or in the groundmass adjacent to Fe-Ti oxide phenocrysts. Two samples were singled out for study and we made numerous thin sections for each of these (Fig. 3, supplementary material figure): i. the only sample that contained numerous zircon crystals, this was, counter-intuitively, the least-evolved andesite and enclave pair, JHS-3 (6 thin sections analysed); and ii. the most-evolved zircon-bearing andesite and enclave pair, JHS-7 (9 thin sections analysed). In JHS-3 the enclave has a chilled contact with the andesite, whereas in JHS-7 the enclave-andesite contact is diffuse.

All zircon analyses were performed in situ on standard polished petrographic thin sections, this permitted determination of the exact compositional and textural position of each analysed grain (Tables 2 and 3).

4. Results

4.1. Whole-rock petrography and geochemistry

Detailed descriptions of the petrography and composition of the SHV mingled andesites and mingled mafic enclaves can be found in Murphy

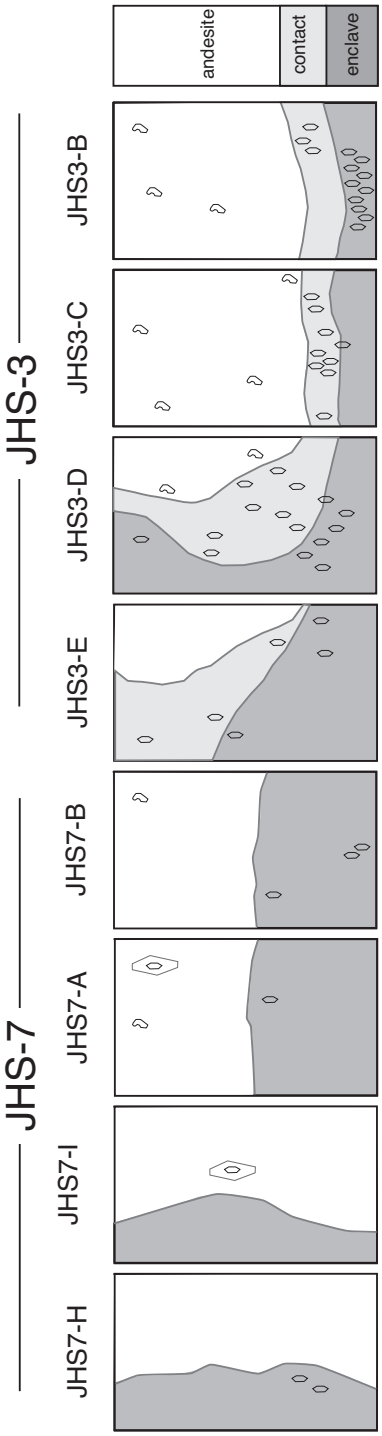

Fig. 3. Compilation of selected multiple copies of the studied thin sections showing where zircon is preserved in the least-evolved, JHS-3, and most-evolved sample JHS-7. Note how in JHS-3 the zircon is preferentially preserved in the quenched contact between the enclave and andesite and that there are many fewer zircon with no indication of preferential preservation in JHS-7. Size of mineral grains exaggerated for clarity. White – andesite, light grey – quenched contact, mid grey – enclave. (See supplementary material figure for zircon position in full thin section set).

et al., (2000); Zellmer et al., (2003a); Christopher et al., (2014); Plail et al., (2018), and references therein. Whole-rock and zircon data are presented in Tables 1–3. Materials and methods are included in a supplementary material file, as is the background rationale for interpretation of the zircon compositional data and a figure showing the distribution of the zircons in thin sections – which is summarized in Fig. 3.

4.1.1. Andesites

The host andesite is compositionally similar in all the eruptive phases. In phase V it is porphyritic and crystal-rich, with 29–38% phenocrysts (Plail et al., 2014). The main phenocryst phases are hornblende, plagioclase, hypersthene and Fe-oxides, with minor clinopyroxene and rounded embayed quartz, accessory minerals are apatite and zircon, the groundmass contains rare rhyolitic glass (Fig. 2e–h; Murphy et al., 2000; Plail, 2014). Amphibole varies from fresh to strongly opacitised and some grains have reaction rims of clinopyroxene, orthopyroxene, plagioclase and oxides. Plagioclase has normal to reverse zoning with sieve textures being common and orthopyroxene crystals are reversely zoned or overgrown by clinopyroxene rims (Murphy et al., 2000). Rare quartz is variably resorbed or has clinopyroxene rims. The groundmass is hypocrystalline, interstitial glass abundance varies from <2% in the least-evolved sample to up to 20% in the most-evolved sample. As detailed above many phenocryst textures indicate disequilibrium.

Table 1
Soufrière Hills Volcano, Montserrat, whole-rock compositions. Major elements are expressed in weight percent, trace elements in ppm. (LOI: loss on ignition.)

	JHS-3 andesite	JHS-3 enclave	JHS-7 andesite	JHS-7 enclave
SiO_2	58.02	49.51	60.55	56.73
TiO_2	0.65	0.89	0.55	0.64
Al_2O_3	18.08	19.90	17.12	18.45
MnO	0.17	0.17	0.18	0.16
MgO	3.18	5.30	2.49	3.24
Fe_2O_3	7.27	9.35	6.48	6.98
CaO	7.52	10.22	6.45	7.78
P_2O_5	0.13	0.11	0.15	0.12
K_2O	0.72	0.54	0.91	0.74
Na_2O	3.41	2.52	3.62	3.28
LOI	−0.16	−0.37	0.22	0.28
Total	99.15	98.51	98.50	98.12
Li	10.8	10.4	13.6	11.9
Rb	10.9	8.5	13.5	12.7
Cs	0.47	0.33	0.63	0.53
Be	0.67	0.46	0.71	0.69
Sr	245	278	233	251
Ba	183	93	213	178
Sc	16.0	28.9	11.0	17.5
V	146	266	103	154
Cr	3.34	4.04	1.39	4.09
Co	24.1	39.6	18.6	48.2
Ni	6.68	13.58	3.41	25.63
Cu	25.4	97.8	46.8	25.8
Zn	66.1	73.7	58.7	69.9
Ga	17.0	18.3	16.1	17.0
Y	21.2	19.4	21.5	20.2
Nb	3.77	2.69	4.04	3.67
Ta	0.39	0.43	0.42	0.65
Zr	90.0	58.0	102.0	91.0
Hf	2.12	1.59	2.26	2.11
Mo	0.91	0.83	1.16	1.00
Sn	0.82	0.98	6.99	1.78
Tl	0.03	0.01	0.16	0.11
Pb	2.47	1.97	3.46	2.58
U	0.70	0.29	0.84	0.69
Th	2.45	0.95	2.88	2.34
La	10.5	5.6	11.6	10.1
Ce	23.0	13.4	25.3	21.8
Pr	2.96	1.93	3.20	2.85
Nd	12.91	9.67	13.85	12.50
Sm	3.27	2.76	3.38	3.11
Eu	1.10	1.05	1.11	1.09
Gd	2.99	3.08	3.05	2.93
Tb	0.54	0.51	0.55	0.52
Dy	3.45	3.35	3.49	3.32
Ho	0.78	0.74	0.78	0.75
Er	2.17	2.05	2.24	2.10
Tm	0.37	0.34	0.38	0.36
Yb	2.39	2.09	2.55	2.35
Lu	0.41	0.34	0.43	0.40

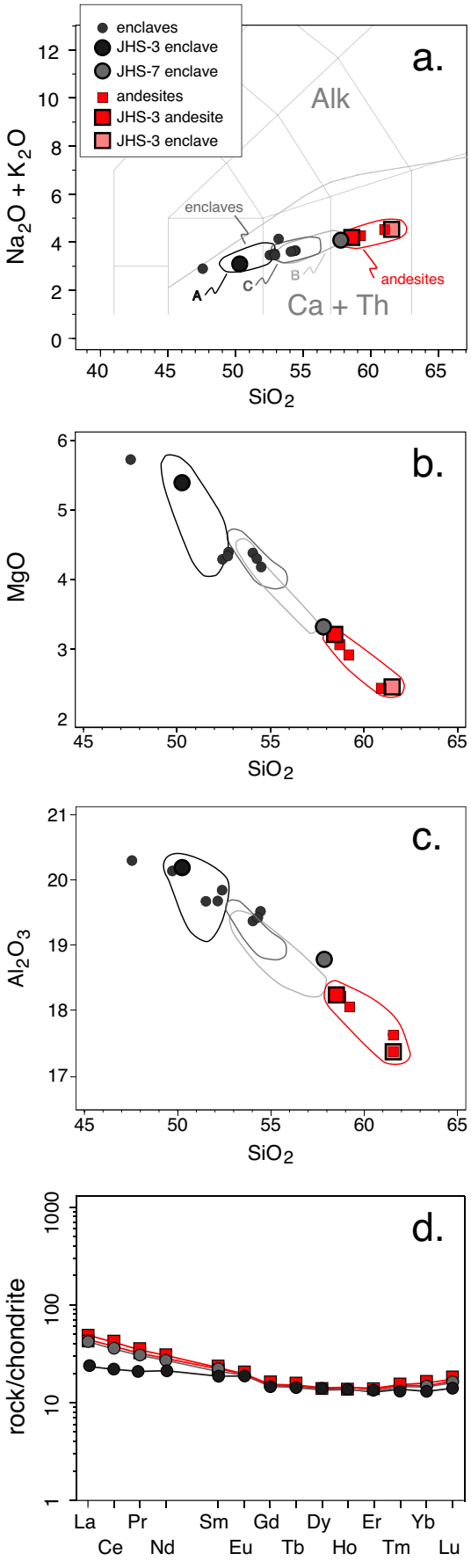

The andesites have a subalkaline, calc-alkaline, metaluminous character SiO_2 58.2–61.5 wt%, $Na_2O + K_2O$ 4.1–4.6 wt%, and a restricted range of MgO 2.4–3.2 wt%, Al_2O_3 17.3–18.3 wt% and K_2O 0.8–0.9 wt% (Table 1 and Fig. 4). Whole-rock major and trace element data plotted versus a differentiation index show linear trends that are attributed to mixing with the enclaves (Plail, 2014). Rare earth elements normalised to chondrite show enrichment in light rare earths (LREE) relative to heavy rare earths (HREE), Eu anomalies are absent or weakly positive-negative (Fig. 4d). Plail et al. (2014) noted no significant change in the composition of andesite erupted in phase V compared to earlier phases.

4.1.2. Enclaves

The mostly phenocryst-poor enclaves comprise a continuous compositional range from basalt to andesite (Murphy et al., 2000; Plail et al., 2014). The only enclave phenocryst phase is plagioclase. The groundmass is composed of plagioclase ± clinopyroxene ± orthopyroxene ± amphibole ± titanomagnetite and ilmenite with varying amounts of interstitial glass (Fig. 2e–h) which is rhyolitic in composition according to Murphy et al. (2000). A diktytaxitic texture is common. Zircon and apatite are accessory minerals. Coarser-grained plagioclase, orthopyroxene, amphibole, and rare quartz grains are phenocrysts 'inherited' from the andesite (Plail, 2014) and show similar resorption and reaction textures to those seen in the host. Plail et al. (2014) divided the enclaves into three groups on the basis of their petrographic and compositional characteristics. Type A is represented by the least-evolved enclave sample JHS-3: highly vesicular (19–40%), up to 5 mm quenched contacts, phenocryst-poor (<9%), and with a fine-grained groundmass. Type B represented by sample JHS-7 is the most-evolved type of enclave: moderately vesicular (9–19%), with diffuse margins, phenocryst-rich (16–26%), and with a fine to medium-grained groundmass. Type C, not included in this study, is a composite of types A and B. The range of enclave types are petrographically distinct from the andesites, but trend towards them compositionally.

The mafic-intermediate enclaves have a subalkaline, tholeiitic, metaluminous character SiO_2 47.5–57.8 wt%, $Na_2O + K_2O$ 2.9–4.3 wt%, and a wide range of MgO 3.3–5.4 wt%, Al_2O_3 18.3–20.4 wt% and K_2O 0.4–8 wt% (Table 1 and Fig. 4). The enclave REE show a range of compositions: normalised to chondrite the least-evolved sample has a flat REE pattern whereas the most-evolved sample is enriched in LREE relative to HREE and overlaps with the andesites (Fig. 4d). Plail et al. (2014) noted a change in the composition of the mafic magma to more Mg- and V-rich over time.

4.2. Zircon

4.2.1. Texture

In both samples selected for study, and where seen albeit rarely in other samples, most zircon grains are equidimensional, a few are elongate (Fig. 5). Almost all zircon crystals are small, ~30–70 μm, in cross-section, but three have dimensions up to 100–200 μm. The grains vary from anhedral to euhedral with pyramidal terminations. All display weak to intermediate cathodoluminescence intensities, some have

Fig. 4. Whole-rock major and trace element data, major elements are expressed in weight percent, trace elements in ppm: a. Total alkalis versus silica diagram for andesites and enclaves from the present study. Larger symbols, samples JHS-3 and JHS-7. The range of andesite compositions from the literature are marked as a field with a red outline, literature data enclave fields for types A, B and C are marked as dark, mid and light grey, respectively. Alk – alkaline, Ca + Th – calc-alkaline and tholeiitic sub-alkaline field. Literature data from Plail (2014), Plail et al., (2014) and Christopher et al. (2014); b. Plot of MgO versus SiO_2, fields and data as in a; c. Plot of Al_2O_3 versus SiO_2, fields and data as in a; d. Chondrite-normalised rare earth element plots, symbols as in a. Normalisation values of McDonough and Sun (1995). (For interpretation of the references to colour in this figure legend, the reader is referred to the web version of this article.)

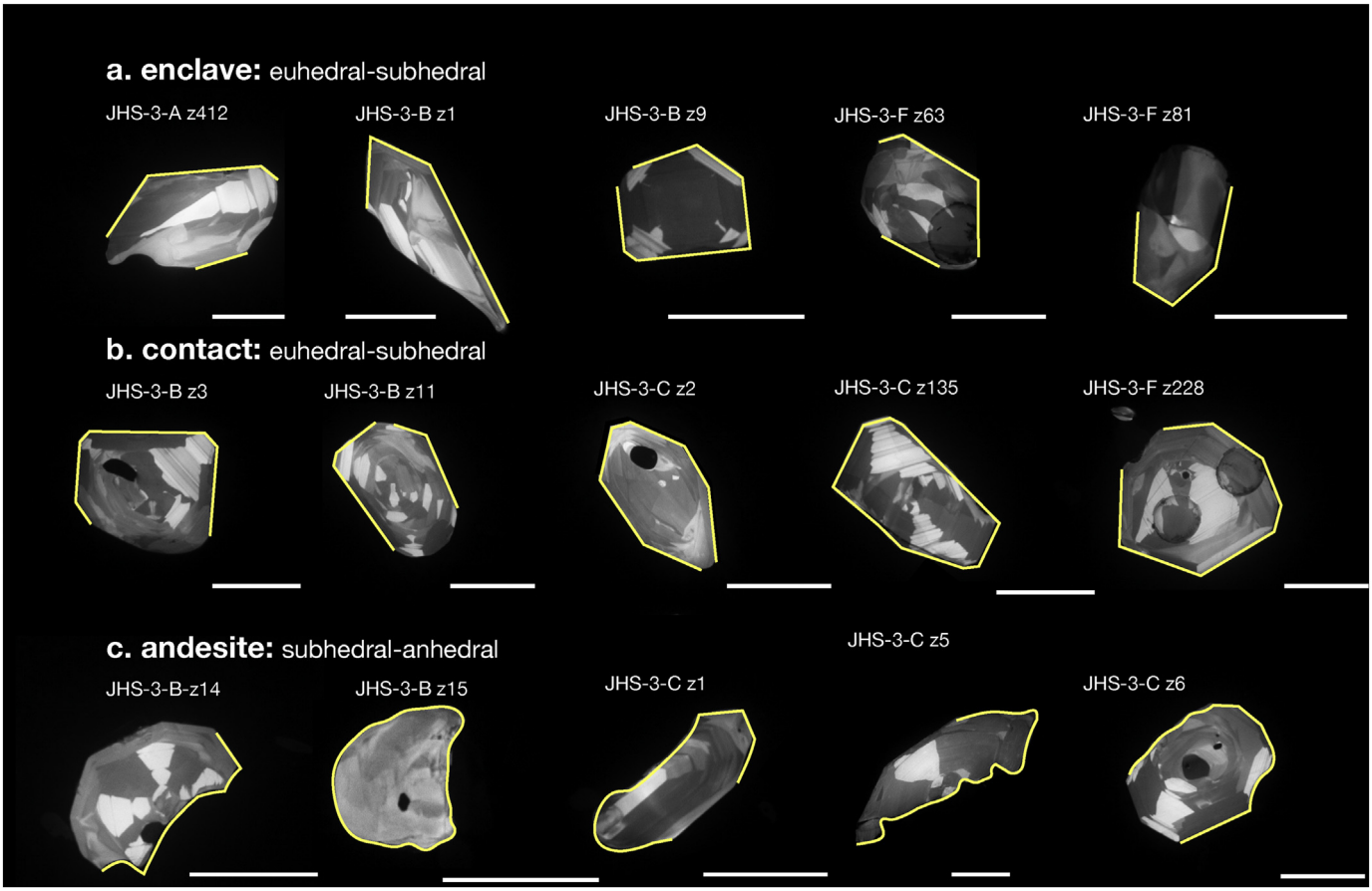

Fig. 5. Selected cathodoluminescence images of typical morphologies of zircon preserved in the least-evolved sample, JHS-3, enclave, contact and andesite. The images highlight the euhedral-subhedral morphology of the enclave and contact zircon that contrasts with the subhedral-anhedral, corroded, shape of the zircon in the andesite. Crystal faces in the enclave and contact zircon and corroded edges in the andesite marked with yellow lines. White bars next to each zircon 50 μm. (For interpretation of the references to colour in this figure legend, the reader is referred to the web version of this article.)

concentric zoning and patchy and sector zoning is common. No distinct cores or rims were identified in any of the crystals.

Detailed petrographic study of numerous thin sections of each of the selected host andesite and enclave pairs revealed intra- and inter-sample zircon distributions that vary substantially (Fig. 3, supplementary material figure). In the least-evolved sample, JHS-3, zircon is preferentially preserved in the quenched contact between the host andesite and enclave. No such enrichment was detected in the most-evolved sample, JHS-7, that has a diffuse contact between the two components, nor in the other, zircon-poor, samples investigated. Remarkably, zircon in the enclaves and quenched contact are predominantly euhedral-subhedral whereas in the andesite groundmass they are typically subhedral-anhedral (Fig. 5).

4.2.2. ^{238}U-^{230}Th zircon crystallisation ages

High-resolution secondary ion mass spectrometry (SIMS) ^{238}U-^{230}Th disequilibrium dating of SHV zircon from andesites and enclaves of the 2010 dome collapse shows that evolved zircon-saturated melts were present in at least some parts of the sub-volcanic magma plumbing system for the last c. 250 ky (Table 2 and Fig. 6). The probability density function for the samples is bimodal with a main peak at c. 45 ka and a subsidiary peak at c. 150 ka. Zircon shows ^{238}U-excesses and ^{230}Th-deficits, plotting to the right of the equiline. $^{238}U/^{232}Th$ activity ratios are between ~5 and 11 with most data plotting in the range between 7 and 10 (Fig. 7). Individual zircon spot analyses ($n = 31$) yielded ^{238}U-^{230}Th zircon-melt isochron model ages from within error of the present-day eruption to c. 250 ka (Fig. 7). No systematic difference is detected in zircon ages in relation to their compositional – least-evolved and most-evolved sample pairs – nor textural – enclave/ contact/andesite – context. Errors on individual zircon ages are comparatively large because U concentrations are low, 37–196 ppm (mean 82 ppm; $n = 31$), nonetheless the U-series dates can resolve a significant age spread >100 ky within a single thin section.

4.2.3. Trace elements

The zircon REE concentrations vary considerably: LREE by up to two orders of magnitude, MREE by an order of magnitude, and HREE by half an order of magnitude (Table 3 and Fig. 8). Despite this, all chondrite-normalised REE patterns are subparallel and depleted in LREE relative to HREE $[Gd/Yb]_N = 0.013–0.034$. The Eu anomalies are weakly to moderately negative with $Eu/Eu^* = 0.28–0.54$ (where $Eu = Eu_N$ and $Eu^* = [Sm \times Gd]_N^{0.5}$) (Fig. 8) compared to absent or weakly positive values for the whole-rocks (Fig. 4). This suggests plagioclase fractionation prior to zircon crystallisation. By contrast, zircon Ce anomalies are strongly positive with $Ce/Ce^* = 7.3–99.1$ (where $Ce = Ce_N$ and $Ce^* = [La \times Pr]_N^{0.5}$) (Fig. 8), but again absent in the whole-rock data (Fig. 4). As with age data, variations in zircon element concentrations are independent of compositional and textural context.

Other zircon trace element concentrations are also heterogeneous, varying from almost typical MORB zircon values $U/Yb < 0.1$, Hf ≤ 9000 ppm, Yb ≤ 500 ppm (Grimes et al., 2015) to much more evolved compositions Hf ~13,400 ppm and Yb ~1400 ppm. They are also independent of compositional context or textural position, as shown by overlapping ratios such as $U/Yb = 0.13–0.20$ and 0.12–0.18 and $Th/U = 0.4–1$ and 0.4–0.8 in the least- and most-evolved samples, respectively (Table 3 and Fig. 9). All zircon U concentrations are low,

Table 2
Soufrière Hills Volcano, Montserrat, U–Th zircon ages.

Sample zircon	Textural position	(^{238}U)/(^{232}Th)	1σ	(^{230}Th)/(^{232}Th)	1σ	m	1σ	Th age ka	1σ + ka	1σ - ka	U ppm
JHS-3-A z412	Enclave	6.83	0.127	3.54	0.382	0.443	0.0657	64.0	13.7	−12.2	86.9
JHS-3-D z1	Contact	8.46	0.153	5.88	0.717	0.658	0.0964	117	36	−27	90.6
JHS-3-D z2a	Contact	7.33	0.132	5.71	0.504	0.749	0.0806	151	42	−30	81.4
JHS-3-D z2b	Contact	7.90	0.166	6.24	0.693	0.764	0.101	158	61	−39	60.1
JHS-3-D z3	Andesite	9.65	0.184	3.42	0.561	0.286	0.0648	36.8	10.4	−9.5	65.4
JHS-3-D z4a	Andesite	5.18	0.101	3.73	0.382	0.661	0.0916	118	34	−26	96.3
JHS-3-D z4b	Andesite	10.1	0.313	5.34	1.050	0.480	0.115	71.4	27.3	−21.8	43.6
JHS-3-D z5a	Enclave	6.98	0.128	3.32	0.418	0.397	0.0699	55.2	13.4	−12.0	80.6
JHS-3-D z5b	Enclave	7.21	0.147	3.28	0.418	0.375	0.0674	51.3	12.5	−11.2	86.7
JHS-3-D z6	Enclave	4.88	0.081	2.28	0.200	0.343	0.0518	45.8	9.0	−8.3	146
JHS-3-D z8	Contact	6.80	0.115	2.32	0.290	0.237	0.0499	29.5	7.4	−6.9	126
JHS-3-D z9	Contact	8.33	0.145	4.26	0.391	0.451	0.0538	65.4	11.3	−10.2	126
JHS-3-D z12	Enclave	9.55	0.169	3.83	0.327	0.338	0.0387	45.0	6.6	−6.2	142
JHS-3-D z13	Enclave	11.0	0.190	4.02	0.417	0.307	0.0419	40.0	6.8	−6.4	124
JHS-3-D z14	Contact	5.14	0.085	2.65	0.197	0.411	0.0480	57.8	9.3	−8.6	145
JHS-3-D z15	Enclave	9.06	0.190	3.77	0.651	0.351	0.0807	47.2	14.5	−12.8	54.9
JHS-3-E z2	Contact	8.51	0.180	7.71	0.920	0.896	0.124	247	∞	−86	53.4
JHS-3-E z4	Contact	7.72	0.131	2.08	0.277	0.170	0.0413	20.4	5.6	−5.3	123
JHS-7-A z193	Enclave	7.45	0.156	3.04	0.610	0.324	0.0942	42.8	16.4	−14.2	73.6
JHS-7-B z196	Enclave	6.05	0.106	1.62	0.351	0.137	0.0691	16.0	9.1	−8.4	65.2
JHS-7-B z196b	Enclave	7.92	0.162	1.14	0.513	0.0305	0.0736	3.38	8.62	−7.99	47.7
JHS-7-B z197	Enclave	5.30	0.089	2.27	0.251	0.308	0.0583	40.2	9.6	−8.8	87.8
JHS-7-B z269a	Enclave	8.16	0.153	3.89	0.599	0.410	0.0836	57.7	16.7	−14.5	51.7
JHS-7-B z269b	Enclave	7.02	0.167	5.52	0.814	0.755	0.136	154	88	−48	37.4
JHS-7-B z269c	Enclave	7.16	0.143	3.94	0.628	0.485	0.102	72.4	24.0	−19.7	39.5
JHS-7-B z269d	Enclave	7.44	0.169	3.42	0.719	0.384	0.111	52.9	21.8	−18.1	36.6
JHS-7-H z2a	Enclave	9.14	0.191	1.91	0.528	0.120	0.0646	14.0	8.3	−7.7	58.5
JHS-7-H z2b	Enclave	7.56	0.128	2.23	0.270	0.196	0.0412	23.9	5.7	−5.5	138
JHS-7-H z2c	Enclave	7.83	0.156	2.32	0.479	0.203	0.0698	24.7	10.0	−9.2	56.0
JHS-7-H z2d	Enclave	9.06	0.223	1.10	0.753	0.0217	0.0928	2.39	10.90	−9.89	35.3
JHS-7-I z1	Andesite	10.8	0.215	6.17	0.675	0.531	0.0694	82.6	17.5	−15.1	85.0

∞ = secular equilibrium.

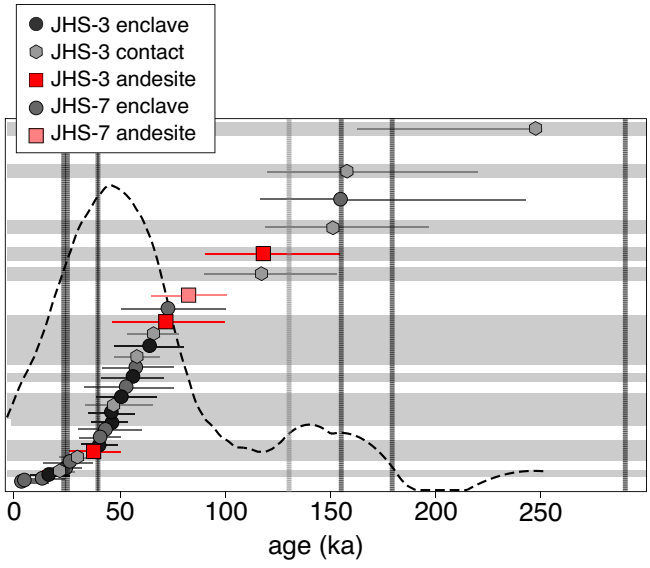

Fig. 6. Probability density function curve and rank order plot showing the distribution of U-Th model ages for zircon crystals from Soufrière Hills Volcano, note the peaks at c. 45 ka and c. 150 ka. Model ages are based on isochron slopes which have symmetrical errors (1σ). Vertical lines are published ^{40}Ar/^{39}Ar ages – see text for details (Section 5.2). Horizontal grey bands highlight ages from the least-evolved sample JHS-3. There is no detectable systematic difference in zircon ages in relation to their compositional – least-evolved and most-evolved sample – nor textural – enclave/contact/andesite – position.

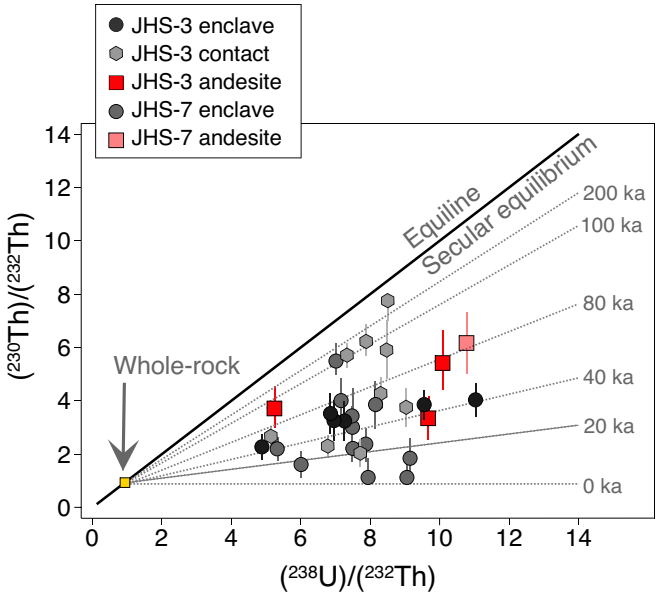

Fig. 7. ^{230}Th/^{232}Th versus ^{238}U/^{232}Th model isochron diagram for Soufrière Hills Volcano zircon. The equiline marks secular equilibrium and is the upper limit of the U-series dating method (c. 375 ka). Error bars plotted as 1σ and truncated at 0 ka.

Table 3
Soufrière Hills Volcano, Montserrat, zircon trace element and Hf isotope data. (nd: not detected).

Sample zircon	Textural position	P	Ca	Ti	Sr	Y	Nb	La	Ce	Pr	Nd	Sm	Eu	Gd	Dy	Er	Yb	Lu	Hf	Ta	Th	U	Zr/Hf	Th/U	Eu/Eu*	Ce/Ce*	$^{176}Lu/^{177}Hf$	2σ	$^{176}Hf/^{177}Hf$	2σ	εHft	2σ
JHS-3-C z1	Contact																										0.0013010	0.00027	0.283174	4.30E-05	13.76	1.52
JHS-3-C z2	Contact	168.0	153	8.1	0.92	693	1.27	0.0110	4.63	0.0380	0.570	1.20	0.630	8.4	48.4	116	435	67.3	9700	0.418	36.1	85.6	50.8	0.422	0.44	33.13	0.0033610	0.00072	0.283165	4.60E-05	13.44	1.63
JHS-3-C z3	Contact																										0.0013900	0.0003	0.283162	3.80E-05	13.33	1.34
JHS-3-C z4	Andesite																										0.0012217	0.00026	0.283157	4.10E-05	13.16	1.45
JHS-3-C z5	Andesite	251.0	145	10.4	1.11	1327	2.54	nd	6.93	0.0930	0.920	2.93	1.070	15.4	90.4	214	828	138.0	11,100	0.700	54.3	111.5	44.4	0.487	0.39	22.56	0.0018450	0.00039	0.283161	4.60E-05	13.30	1.63
JHS-3-C z6	Andesite																										0.0012210	0.00026	0.283132	3.80E-05	12.27	1.34
JHS-3-C z135	Contact	186.0	149	3.9	nd	871	1.16	0.0160	4.27	0.0580	1.110	2.76	0.960	15.3	69.0	141	461	73.0	11,300	0.283	48.8	88.4	43.6	0.552	0.36	20.12	0.0008728	0.00019	0.283143	4.10E-05	12.66	1.45
JHS-3-C z136	Contact																										0.0011170	0.00024	0.283161	4.10E-05	13.30	1.45
JHS-3-C z146	Contact	181.0	270	8.5	1.07	823	1.74	0.1800	5.21	0.0840	1.240	2.10	0.880	13.2	61.5	131	464	72.0	10,260	0.388	42.8	73.5	48.1	0.582	0.39	10.21	0.0014750	0.00031	0.283181	3.90E-05	14.01	1.38
JHS-3-C z147	Contact																										0.0015920	0.00033	0.283128	3.90E-05	12.13	1.38
JHS-3-C z212	Contact	167.0	220	8.2	nd	739	1.5	nd	4.45	0.0150	0.490	1.22	0.500	8.4	51.1	122	467	76.4	9160	0.463	31.5	81.5	53.8	0.387	0.35	89.82	0.0010138	0.00021	0.283151	4.70E-05	12.94	1.66
JHS-3-C z264	Andesite	230.0	163	6.9	0.95	1166	1.9	nd	6.52	0.0350	0.460	2.08	0.920	12.0	77.2	198	726	116.0	9500	0.552	49.5	121.0	51.9	0.409	0.44	56.40	0.0004990	0.00011	0.283143	4.20E-05	12.66	1.49
JHS-3-D z1	Contact																										0.0009550	0.00012	0.283198	4.10E-05	14.61	1.45
JHS-3-D z2a	Contact	151.0	nd	4.1	0.93	635	1.07	0.1600	3.89	0.0430	1.190	1.39	0.610	9.5	48.9	108	349	60.7	11,700	0.310	30.4	49.0	42.1	0.620	0.38	11.15	0.0010060	0.00011	0.283194	5.20E-05	14.47	1.84
JHS-3-D z2b	Contact	146.0	nd	5.7	nd	586	1.38	nd	3.69	0.0180	0.460	0.85	0.450	6.4	43.9	106	333	62.5	11,500	0.282	26.2	52.9	42.9	0.495	0.42	62.07	0.0008220	8.40E-05	0.283179	5.10E-05	13.94	1.80
JHS-3-D z3	Andesite	213.0	nd	4.7	0.64	850	0.82	nd	3.84	0.0490	0.930	2.37	0.740	13.0	65.2	137	452	81.3	11,700	0.376	39.2	65.3	42.1	0.600	0.32	23.73	0.0011340	0.00012	0.283184	4.40E-05	14.11	1.56
JHS-3-D z4a	Andesite	152.0	nd	4.6	nd	466	0.88	nd	3.31	0.0130	0.230	0.84	0.275	5.8	32.5	79	276	49.3	12,300	0.275	23.9	52.8	40.1	0.453	0.28	77.09	0.0006310	6.70E-05	0.283239	4.30E-05	16.06	1.52
JHS-3-D z4b	Andesite	100.0	nd	3.3	nd	354	1.16	nd	2.72	0.0100	0.220	0.48	0.280	5.0	27.7	62	233	41.0	12,000	0.179	15.5	37.4	41.1	0.414	0.35	82.35	0.0005450	5.70E-05	0.283175	4.10E-05	13.79	1.45
JHS-3-D z5a	Enclave	367.0	nd	4.1	0.68	1690	1.68	nd	8.10	0.0880	2.390	6.00	2.580	30.5	135.0	275	930	154.0	10,700	0.530	120.0	159.0	46.1	0.755	0.47	27.87	0.0014940	0.00016	0.283172	4.50E-05	13.69	1.59
JHS-3-D z5b	Enclave	324.0	nd	4.1	nd	980	0.85	nd	4.80	0.0340	1.170	2.68	1.250	14.6	76.0	163	570	104.0	10,600	0.208	55.0	85.0	46.5	0.647	0.49	42.74	0.0015600	0.00018	0.283164	4.70E-05	13.40	1.66
JHS-3-D z6	Enclave	271.0	nd	3.6	0.80	948	1.08	nd	4.13	0.0810	1.270	2.89	1.130	13.2	71.9	155	505	94.8	12,700	0.376	48.4	76.7	38.8	0.631	0.47	15.44	0.0015500	0.00021	0.283169	4.90E-05	13.58	1.73
JHS-3-D z8	Contact																										0.0012390	0.00015	0.283086	5.40E-05	10.65	1.91
JHS-3-D z9	Contact																										0.0015360	0.00016	0.283190	5.70E-05	14.32	2.02
JHS-3-D z12	Enclave																										0.0016400	0.00017	0.283139	6.70E-05	12.52	2.37
JHS-3-D z13	Enclave	254.0	nd	nd	0.76	1420	2.27	nd	7.62	0.0860	1.380	3.66	1.210	17.1	103.6	236	824	147.0	11,400	0.660	77.9	144.0	43.2	0.541	0.39	26.83	0.0019500	0.0002	0.283130	6.40E-05	12.20	2.26
JHS-3-D z14	Contact																										0.0018300	0.00019	0.283189	5.90E-05	14.29	2.09
JHS-3-D z15	Enclave																										0.0006100	6.20E-05	0.283240	1.10E-04	16.09	3.89
JHS-3-F z28	Enclave	118.6	197	5.9	0.67	595	0.86	0.1780	3.63	0.0730	1.190	1.84	0.860	11.6	47.2	93	335	53.3	10,410	0.256	26.7	44.5	47.4	0.600	0.43	7.70	0.0008570	0.00019	0.283177	3.90E-05	13.86	1.38
JHS-3-F z60	Enclave	292.0	200	8.3	1.05	2790	2.14	0.0420	13.40	0.3180	5.030	11.80	5.580	59.3	255.0	445	1400	204.0	9860	0.610	195.0	196.0	50.0	0.995	0.52	12.13	0.0003250	7.30E-05	0.283170	3.80E-05	13.62	1.34
JHS-3-F z63	Enclave	230.0	164	9.0	0.80	1330	1.8	0.0550	7.89	0.1080	1.270	3.36	1.810	19.2	101.0	205	801	116.0	7890	0.490	78.5	137.0	62.5	0.573	0.54	18.44	0.0009839	0.0002	0.283117	4.00E-05	11.74	1.41
JHS-3-F z81	Enclave	170.0	204	7.7	0.83	650	1.29	0.0028	3.50	0.0520	0.470	1.68	0.720	9.8	52.7	104	398	61.0	9300	0.293	32.0	58.3	53.0	0.549	0.42	19.96	0.0017510	0.00037	0.283133	3.90E-05	12.31	1.38
JHS-3-F z136	Contact																										0.0014800	0.00033	0.283156	3.50E-05	13.12	1.24
JHS-3-F z148	Contact	141.0	185	5.8	0.60	571	1.34	nd	3.52	0.0360	0.750	1.55	0.630	9.0	44.7	94	342	53.5	9760	0.195	28.7	54.8	50.5	0.524	0.40	29.60	0.0019690	0.00042	0.283158	4.70E-05	13.19	1.66
JHS-3-F z174	Contact	192.0	164	7.9	nd	870	1.99	nd	5.51	0.0240	0.440	1.98	0.800	10.6	64.6	151	612	96.1	9700	0.470	37.6	90.2	50.8	0.417	0.43	69.51	0.0011370	0.00024	0.283122	4.30E-05	11.92	1.52
JHS-3-F z198	Contact	202.0	286	8.7	1.04	1040	1.07	0.0580	4.69	0.1360	1.900	3.60	1.650	18.9	84.6	169	557	83.2	8750	0.374	50.8	89.0	56.3	0.571	0.49	8.95	0.0014640	0.00031	0.283148	3.90E-05	12.84	1.38
JHS-3-F z228	Contact																										0.0013608	0.00027	0.283159	5.10E-05	13.23	1.80
JHS-3-F z282	Contact	216.0	275	7.3	nd	795	0.92	0.0036	3.96	0.0540	0.790	1.83	1.040	13.2	61.4	125	491	70.6	9500	0.306	33.0	66.6	51.9	0.495	0.47	21.64	0.0013930	0.0003	0.283142	3.80E-05	12.63	1.34
JHS-3-F z325	Andesite																										0.0007280	0.00015	0.283164	4.30E-05	13.40	1.52
JHS-3-F z379	Andesite	129.0	164	7.1	nd	801	1.16	0.0100	4.07	0.0600	1.370	2.67	1.190	14.1	65.5	125	447	69.1	10,120	0.273	40.4	66.2	48.7	0.610	0.48	19.28	0.0015870	0.00032	0.283151	3.90E-05	12.94	1.38
JHS-3-F z399	Andesite																										0.0014470	0.0003	0.283137	4.70E-05	12.45	1.66
JHS-3-F z417	Andesite																										0.0008500	0.00021	0.283157	4.40E-05	13.16	1.56
JHS-7-A z10	Andesite																										0.0017680	0.00016	0.283148	3.80E-05	12.84	1.34
JHS-7-A z18	Andesite																										0.0012150	0.00012	0.283202	7.90E-05	14.75	2.79
JHS-7-A z193a	Enclave																										0.0009860	0.0001	0.283175	3.80E-05	13.79	1.34
JHS-7-A z193b	Enclave																										0.0008670	8.10E-05	0.283142	6.60E-05	12.63	2.33
JHS-7-B z196a	Enclave																										0.0011830	0.00011	0.283166	6.60E-05	13.48	2.33
JHS-7-B z196b	Enclave	187.0	nd	nd	0.89	1100	1.09	nd	4.71	0.0310	1.600	3.85	1.510	18.7	89.1	176	567	90.0	11,500	0.460	43.8	75.0	42.9	0.584	0.45	46.00	0.0007888	7.20E-05	0.283153	6.50E-05	13.02	2.30
JHS-7-B z197	Enclave																										0.0011000	0.0001	0.283161	5.90E-05	13.30	2.09
JHS-7-B z269a	Enclave	127.0	nd	nd	nd	492	0.82	0.0250	3.35	0.0500	0.270	1.60	0.380	6.6	36.2	81	301	54.7	11,800	0.259	26.0	51.0	41.8	0.510	0.31	16.96	0.0008056	7.40E-05	0.283126	6.40E-05	12.06	2.26
JHS-7-B z269b	Enclave	121.0	nd	nd	nd	740	0.82	0.1540	4.14	0.0570	1.180	2.17	0.970	14.2	57.2	120	384	65.4	13,400	0.268	40.6	69.0	36.8	0.588	0.40	10.69	0.0008770	8.20E-05	0.283157	6.60E-05	13.16	2.33
JHS-7-B z269c	Enclave																										0.0007360	7.30E-05	0.283125	6.10E-05	12.03	2.16
JHS-7-B z269d	Enclave																										0.0008441	7.70E-05	0.283183	8.80E-05	14.08	3.11
JHS-7-C z309	Enclave	172.0	136	8.2	nd	706	1.33	nd	4.08	0.0140	0.450	1.28	0.660	8.8	47.1	123	453	75.6	10,280	0.520	26.3	62.6	48.0	0.420	0.44	88.24	0.0007340	7.10E-05	0.283178	3.40E-05	13.90	1.20
JHS-7-C z312	Andesite																										0.0018240	1.70E-04	0.283215	3.90E-05	15.21	1.38
JHS-7-C z352	Enclave																										0.0015910	1.60E-04	0.283158	3.80E-05	13.19	1.34
JHS-7-C z372	Enclave																										0.0014090	1.40E-04	0.283173	3.60E-05	13.72	1.27
JHS-7-C z373	Enclave	218.0	141	7.7	nd	917	0.95	0.1650	4.80	0.1340	1.870	3.34	1.070	15.1	67.5	151	499	84.7	10,810	0.379	47.8	77.1	45.6	0.620	0.39	7.32	0.0013570	0.00014	0.283152	3.30E-05	12.98	1.17
JHS-7-C z379	Enclave	235.0	139	13.2	0.82	1430	2.47	0.0790	8.05	0.1070	1.290	2.20	1.010	14.7	96.9	238	826	134.0	9780	0.750	69.1	126.8	50.4	0.545	0.40	17.67	0.0020080	0.00018	0.283172	3.70E-05	13.69	1.31
JHS-7-D z185	Andesite																										0.0022540	0.00021	0.283188	3.50E-05	14.25	1.24
JHS-7-E z4	Andesite																										0.0016210	0.00015	0.283174	3.20E-05	13.76	1.13
JHS-7-E z12	Andesite																										0.0017360	0.00016	0.283143	3.60E-05	12.66	1.27
JHS-7-E z79	Andesite																										0.0015570	0.00015	0.283147	3.50E-05	12.80	1.24
JHS-7-E z138	Enclave																										0.0020470	0.00019	0.283135	3.30E-05	12.38	1.17
JHS-7-E z162	Enclave																										0.0008680	8.20E-05	0.283173	3.80E-05	13.72	1.34
JHS-7-F z1b	Andesite	189.0	1500	nd	2.40	1470	nd	0.0360	5.60	0.1500	3.000	4.90	2.100	26.3	127.0	236	620	116.0	11,400	0.190	87.0	111.0	43.2	0.784	0.45	10.33	0.0024640	0.00023	0.283140	7.30E-05	12.56	2.58
JHS-7-G z2a	Andesite	244.0	nd	nd	1.50	1150	1.31	0.0180	4.60	0.1140	1.340	3.60	1.350	21.9	91.0	181	550	117.0	13,200	0.385	45.1	67.0	37.3	0.673	0.36	11.51	0.0013970	0.00013	0.283179	6.70E-05	13.93	2.37
JHS-7-G z2b	Andesite	174.0	nd	nd	1.95	810	1.86	0.1100	4.03	0.0360	0.470	0.96	0.570	7.0	48.5	132	390	91.0	10,880	0.260	25.6	65.0	45.3	0.394	0.49	15.43	0.0014640	0.00014	0.283148	8.40E-05	12.84	2.97
JHS-7-H z2a	Enclave																										0.0005860	5.80E-05	0.283174	6.80E-05	13.76	2.40
JHS-7-H z2b	Enclave																										0.0011000	0.00015	0.283114	7.00E-05	11.64	2.48
JHS-7-H z2c	Enclave	196.0	nd	nd	0.96	795	1.44	nd	4.91	0.0150	0.540	1.37	0.680	10.1	57.2	124	464	77.3	11,000	0.514	32.1	76.7	44.8	0.419	0.40	99.11	0.0007902	7.20E-05	0.283112	6.50E-05	11.57	2.30
JHS-7-H z2d	Enclave																										0.0008140	7.90E-05	0.283146	7.20E-05	12.77	2.55
JHS-7-I z1	Andesite	169.0	nd	nd	nd	646	0.96	nd	3.43	0.0300	0.730	1.83	0.820	10.8	48.3	106	354	60.1	10,900	0.247	26.6	60.0	45.2	0.443	0.44	34.62	0.0006830	9.60E-05	0.283103	6.90E-05	11.25	2.44

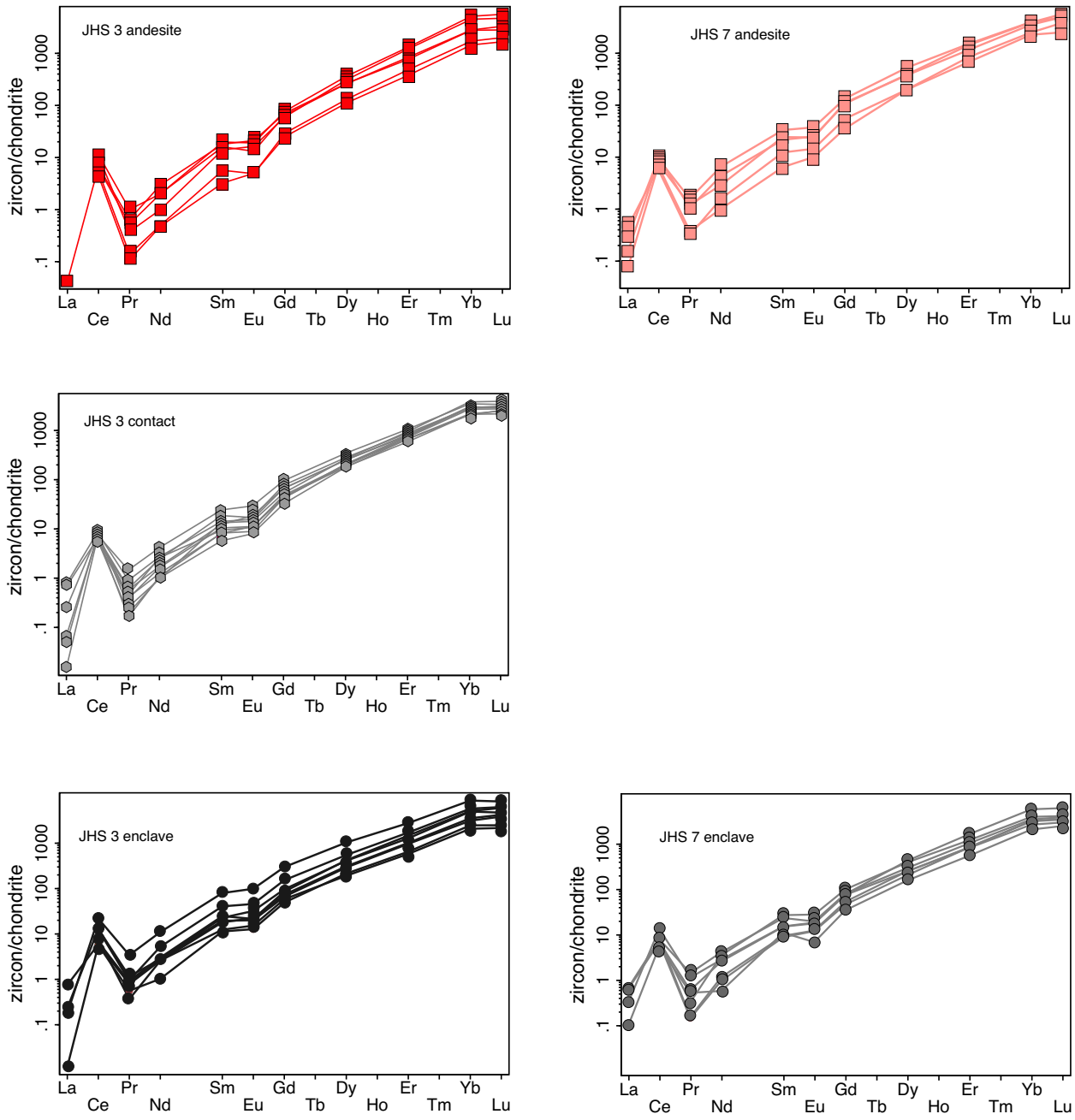

Fig. 8. Zircon chondrite-normalised rare earth element plots. All samples show a pronounced positive anomaly in Ce and a negative anomaly in Eu. Normalisation values of McDonough and Sun (1995). The REE concentrations do not vary in relation to their compositional – least-evolved and most-evolved sample – nor textural – enclave/contact/andesite – position. Trace elements expressed in ppm.

37–196 ppm. As zircon crystallises and fractionates Zr becomes relatively more depleted in the melt compared with the slightly less compatible Hf, so the abundance of Hf in the melt and consequently subsequently crystallising zircon increases. For this reason, zircon Zr/Hf can be used as an index of melt differentiation, with the lowest values expected in evolved melts that have lower Zr and higher Hf (Claiborne et al., 2006a). Notably, zircon from both the least- and most-evolved samples have overlapping broad Zr/Hf ranges of 38.8–53.8 (with two values up to 62.5) and 30.2–50.4, respectively. For the zircon dataset as a whole, Zr/Hf correlates positively with Ti and Eu/Eu* (Fig. 9). Few zircon crystals were dated and errors on ages are large, so it is difficult to make a clear assessment systematic of variation in zircon trace element compositions over time but no clear correlations with age were observed for the available data (Fig. 10).

The trace element data show that Montserrat zircon plots in the island-arc field of the Grimes et al. (2015) U/Yb vs Hf tectonomagmatic discrimination diagram (Fig. 11). It should be noted that the island-arc field was defined using zircon from ophiolites, but subsequent studies have verified its position using arc-related detrital zircon (e.g., Breitkreuz et al., 2021). To the best of our knowledge, the new results presented here are the first zircon data from a currently erupting system to confirm the validity of the island-arc field in this tectonomagmatic discrimination diagram.

4.2.4. Hf isotopes

Zircon Hf isotope ratios are sensitive to variations in magma source composition, with depleted mantle displaying high εHf values whereas more enriched sources, such as continental crust or sediment derived

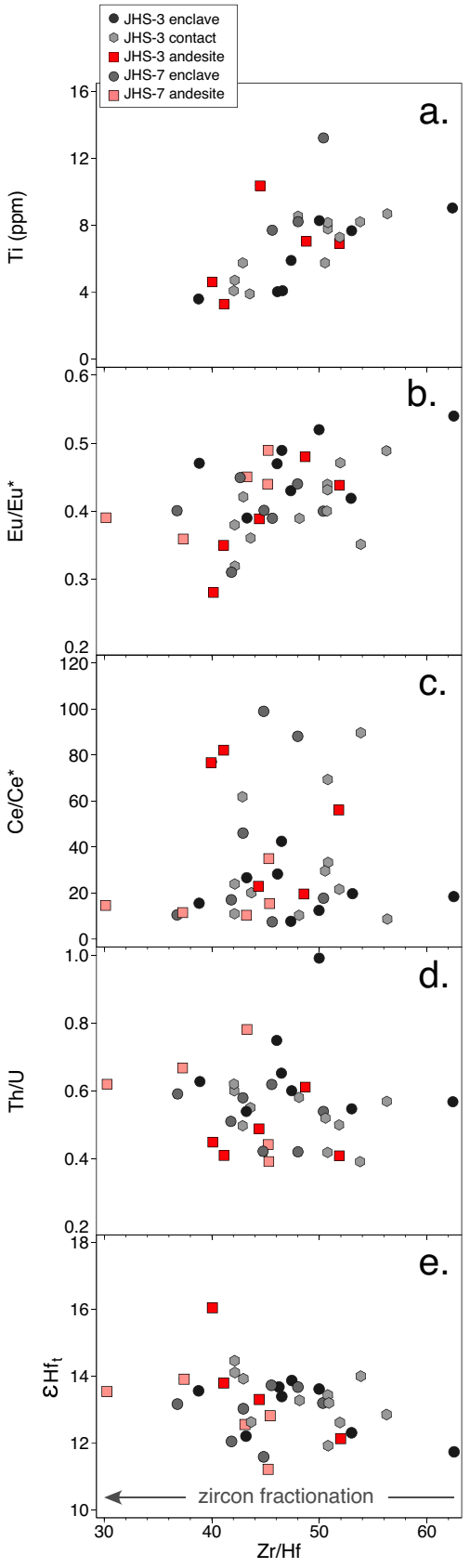

Fig. 9. Zircon trace element concentrations, element ratios and Hf isotope compositions versus differentiation index Zr/Hf: a. Ti; b. Eu/Eu*; c. Ce/Ce*; d. Th/U; e. εHf. Only Ti and Eu/Eu*, the latter lowered by plagioclase fractionation, correlate with Zr/Hf, no other trace element concentrations nor ratios do. All elements expressed in ppm.

from it, have mostly negative values (Pettingill and Patchett, 1981). It is significant, therefore, that within the determined uncertainties, all SHV zircon is compositionally indistinguishable. Zircon εHf varies by <3 units (with one exception taking the spread to 5 units): from 11.3 ± 1.2 to 16.1 ± 1.9 (n=35, 2σ standard error). In addition, both samples have the same zircon εHf averages within uncertainty: 13.3 ± 0.5 (n=23) for the least-evolved sample and 13.5 ± 0.5 (n = 12) for the most-evolved. Therefore, as seen in the age and trace element data, there is no systematic compositional difference in the Hf isotopes of zircon preserved in the andesites, contacts or enclaves (Fig. 12). Nor do the εHf values correlate with differentiation, Zr/Hf, or age (Figs. 9 and 10).

The Montserrat zircon εHf compositions plot at 13.3 ± 0.5 (2σ) at 0 ka, exactly the composition expected based on the continental crust Hf isotope evolution line that was recently defined using whole-rock data from modern island arcs (Fig. 13) (Dhuime et al., 2011). Remarkably, magmatic zircon from currently erupting arc systems are not plotted in any of the 200 plus papers that cite Dhuime et al. (2011). So, once more, our data are the first to confirm the validity of the plot.

4.2.5. Intensive variables

Zircon crystallisation temperatures can be calculated from Ti contents if melt Si and Ti activity, aSiO$_2$ and aTiO$_2$, are known (Ferry and Watson, 2007). Given that quartz is present in both host lava and enclaves, albeit sparsely and as rounded embayed crystals, aSiO$_2$ = 1 is reasonably assumed. If quartz was not in equilibrium with the melt from which the zircon crystallised, however, aSiO$_2$ < 1 would increase the calculated temperatures, e.g., by ~50°C for aSiO$_2$ = 0.5. A relatively high value of aTiO$_2$ can also be inferred as both titanomagnetite and ilmenite are present in both rock types. Host andesite and enclave aTiO$_2$, oxygen fugacity, fO$_2$, and temperature were calculated for phase V ilmenite and titanomagnetite compositions from Christopher et al. (2014). Using the equations of Ghiorso and Gualda (2013) the andesite titanomagnetite microphenocrysts cores, rims and groundmass microlite compositions all gave an aTiO$_2$ of 0.7 and log10fO$_2$ + 1.15 relative to FMQ (O'Neill and Pownceby, 1993), compared to NNO +1.65, FMQ equivalent +1.96, calculated by Christopher et al. (2014). The Fe-Ti oxide temperature varied between the core compositions 860°C and the rims and groundmass 830°C. In the enclaves the aTiO$_2$ was also 0.7 with log$_{10}$$f$O2 + 1 relative to FMQ and an Fe-Ti oxide temperature of 830°C was calculated.

The SHV Ti-in-zircon crystallisation temperatures range from 680°C to 785°C, calculated using the equations of Ferry and Watson (2007), typical error for this composition and temperature range are ~5%. However, they lack significant departures to higher temperatures and are always below the Fe-Ti oxide temperatures. There is no clear difference in the range of zircon crystallisation temperatures between the andesites host, 708–785°C, contact, 694–767°C, or enclaves, 680–770°C. Counter-intuitively, the average temperature of zircon from the least-evolved sample, 733°C, is lower than that from the most-evolved sample, 775°C. Nevertheless, independent of the absolute temperatures, the zircon thermometry dataset as a whole shows: a strong positive correlation with Zr/Hf; moderate positive correlations with U, Nb, Ta and REE; moderate-weak positive correlations with Eu/Eu* and Sr; and a strong negative correlation with Hf concentrations but not εHf values (Fig. 14).

Magma composition, in particular Zr content, M value (cation ratio (Na + K + 2Ca)/(Al · Si)) and temperature control zircon crystallisation (Watson and Harrison, 1983). The SHV whole-rock zircon saturation temperatures (ZST), calculated the using the equations of Boehnke et al. (2013) are low, ranging from 555°C for the least-evolved enclave to 620°C for the most-evolved, and similarly from 620°C for the least-evolved andesite to 650°C for the most-evolved. However, considerable

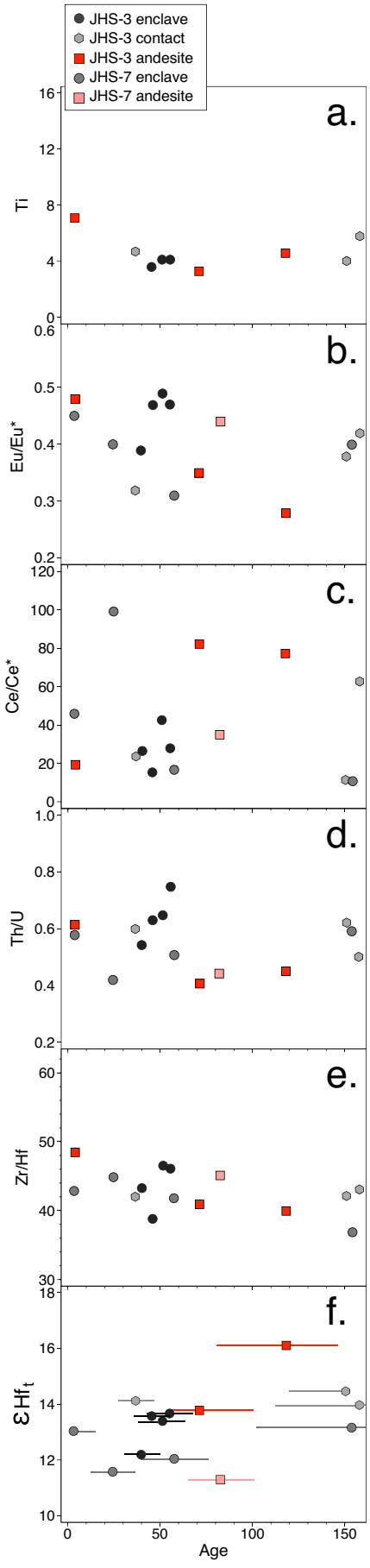

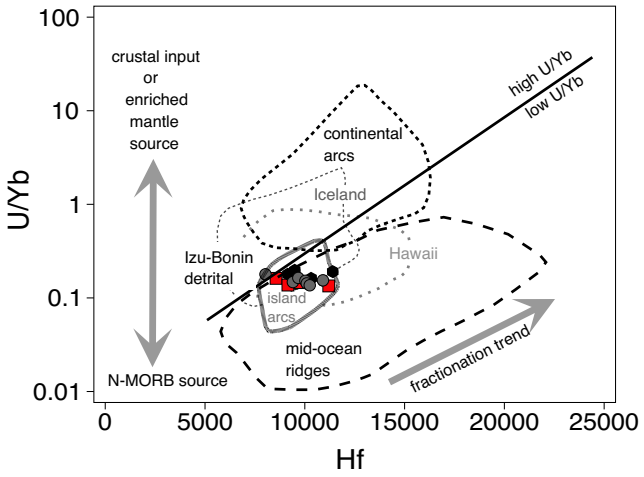

Fig. 11. U/Yb vs Hf tectonomagmatic discrimination diagram of Grimes et al. (2015). All the Montserrat zircon plots in the island arc field irrespective of compositional – least-evolved and most-evolved sample – or textural – enclave/contact/andesite – position. To the best of our knowledge, the new data presented here are the first zircon from an actively erupting system to confirm the validity of this field. All elements expressed in ppm.

temperature underestimation can result from whole-rock compositions being non-representative of melt compositions (Harrison et al., 2007).

5. Discussion

5.1. Zircon as a record of magma processes at different length scales

Melt and mineral residence times and volumes of magma in subvolcanic reservoirs define the potential of the system to erupt and eruption size, thus controlling the associated hazard and risk. In the current controversy over warm – melt dominated – versus cold – crystal dominated – magma storage both scenarios are end-member alternatives and natural systems will display a continuum between them (Cooper, 2019). Heterogeneous transcrustal magma systems crystal cargoes are stored in a long-lived mush and then incorporated into melt shortly before eruption (Cashman et al., 2017). An important implication of this is that intracrustal melt is commonly present in magma reservoirs below dormant volcanoes and is not, in itself, sufficient to indicate impending eruption (Barboni et al., 2016). In a recent comprehensive review of magma reservoir architecture and dynamics Edmonds et al. (2019) highlighted the complexity of such systems and the need for new models, first, to understand magma fluxes, i.e., timescales and volumes and, second, to determine how such data may be used in forecasting. Temporal constraints are needed to develop more realistic magma reservoir models that reflect natural complexities. In particular, questions remain regarding where crystals and melt are stored, for how long, and how this controls when magma may erupt. This information is crucial to understand potential future eruption dynamics. Cashman et al. (2017) also reasoned that investigation of the variable crystal cargoes of erupted magmas will advance understanding of the spatial and temporal evolution of magmatic systems. Below we discuss how i. our SHV new zircon ages record magmatic system longevity greater than any other mineral and, ii. the zircon compositional data provide information about the physical and compositional state of the magmatic plumbing

Fig. 10. Zircon trace element concentrations, element ratios and Hf isotope compositions versus age: a. Ti; b. Eu/Eu*; c. Ce/Ce*; d. Th/U; e. Zr/Hf; f. εHf. No clear correlations with age were observed in these or other elements or ratios. All elements expressed in ppm. Age error bars plotted as 1σ in f. and truncated at 150 ka.

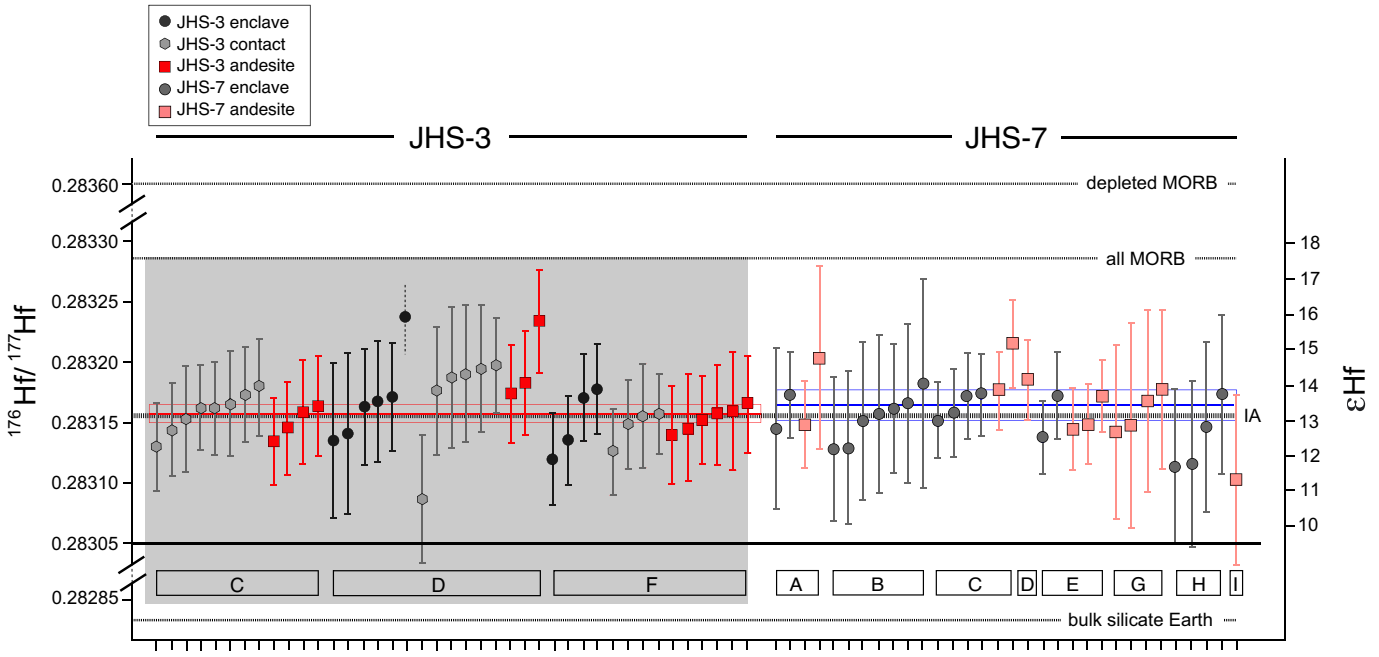

Fig. 12. Zircon $^{176}Hf/^{177}Hf$ ratios, all the data are within error (2σ), independent of the compositional – least-evolved and most-evolved sample – or textural – enclave/contact/andesite – position. The grey box highlights the analyses from the least-evolved sample, JHS-3. Letter bars at base refer to the specific JHS-3 and JHS-7 sample thin sections.

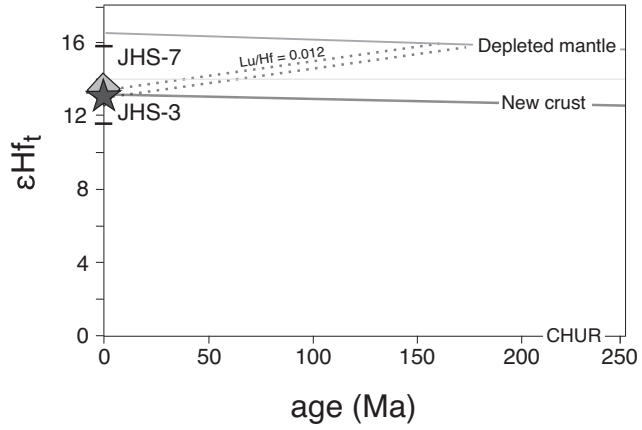

Fig. 13. Plot of εHf versus age showing the hafnium isotope evolution of the depleted mantle (DM) and of new continental crust (NC) from Dhuime et al. (2011). The DM linear evolution is of a chondritic uniform reservoir (CHUR) value since the formation of the Earth, 0 at 4.56 Ga to εHf = 17. The NC evolution curve is for linear evolution from the same reservoir to εHf = 13.2 for the new crust. Dhuime et al. (2011) fixed the composition of the present-day new continental crust as the weighted average of whole-rock εHf, 13.2, of sample means from 13 arcs. The SHV zircon εHf means of both the least- and most-evolved samples, JHS-3 and JHS-7 respectively, plot at 0 ka, 13.3 ± 0.5, on the new continental crust line.

system from millennial decametre-kilometre-scale transcrustal magma storage to recent centimetre-scale magma mingling.

5.2. Insights into magmatic processes from zircon geochronology: transcrustal magma storage – timing of crystals and melt

As noted by Cooper (2015) crystals in magmatic rocks track temporal variations in dynamic processes in crustal magma reservoirs, often registering the entire history of a volcanic centre. Magmatic zircon antecrysts – crystals that did not crystallise from the host magma but are petrogenetically related to the same system – are particularly useful in this respect. They may have protracted pre-eruptive histories recording <1000 to 100,000s of years of magma accumulation and residence thus tracking mineral recycling processes and constraining the age range of magmatic components (Schmitt, 2011; Cooper, 2015).

Considering the longevity of the SHV magmatic system, Murphy et al. (2000) concluded that magmas erupted since c. 18 ka were derived from the same relatively old, highly crystalline magma reservoir on the basis of: their crystal-rich nature; similarity in whole-rock compositions; petrography; and relatively low calculated magma temperatures. They noted that periodic perturbation of the system by influx of hotter mafic magma was recorded by enclaves, similar to the recent SHV activity. More broadly, the compositional and petrographic similarity of the recent activity with SHV volcanic rocks erupted over the last c. 170 ky was inferred by Zellmer et al. (2003b). From similarities in whole-rock Pb isotope compositions Cassidy et al. (2012) tentatively proposed that the SHV magmatic activity may have extended back to 280 ka rather than 174 ka as previously concluded (Harford et al., 2002).

Our new zircon ^{238}U-^{230}Th disequilibrium ages record zircon crystallisation in a melt-mush system which contained more evolved melt than represented by the erupted andesite. This confirms that the SHV 1995–2010 volcanic activity sampled a magma reservoir that was active over c. 250 ka. Throughout its history, at least some parts of the SHV magma system were sufficiently cold and evolved to become saturated in zircon. The sparsity of eruption age zircon, however, suggests the bulk composition of both the host andesites and enclaves magmas were zircon undersaturated, although multiple dissolution and overgrowth textures have not been observed. Ages vary considerably by >100 ky in a single petrographic thin section. This indicates preservation of zircon that crystallised from distinct melt lenses and were subsequently stored below or near the solidus then amalgamated as antecrystic crystal cargoes at some point prior to eruption. Then, mixing between zircon crystals of different age and provenance occurred during mush destabilisation in the shallow parts of a transcrustal magma systems (cf., Cashman et al., 2017). Hence, the range of zircon ages found in any given sample are, to a great extent, arbitrary and dependent on the mush zone regions that were remobilised. Zircon incorporated into a Zr-undersaturated melt will be resorbed over time, for example by intermittent hot, mafic, magma recharge, so younger, or more recently incorporated crystals – of any age – may be preferentially preserved in erupted products.

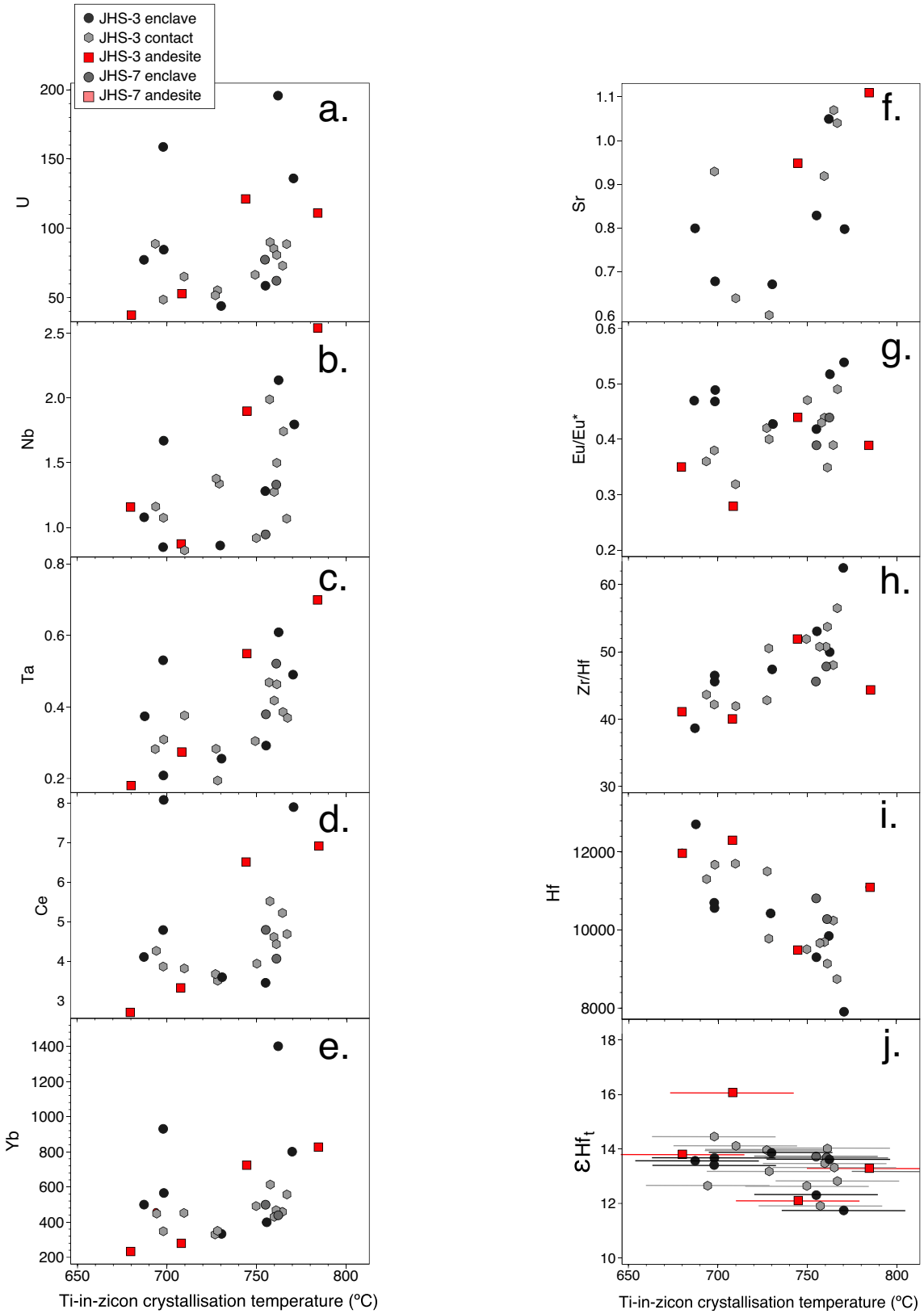

Fig. 14. Zircon trace element concentrations, element ratios and Hf isotope compositions versus Ti-in-zircon crystallisation temperature (°C): a. U; b. Nb; c. Ta; d. Ce; e. Yb; f. Sr; g. Eu/Eu*; h. Hf; i. Zr/Hf; j. εHf. Uranium, Nb, Ta, the REE, Sr and Eu/Eu* as well as Zr/Hf correlate positively with Ti-in-zircon crystallisation temperature, by contrast Hf correlates negatively, εHf does not correlate. Error bars shown in j., 5%, correlations are independent of the absolute temperature. All elements expressed in ppm.

The zircon U-Th results tie in with published $^{40}Ar/^{39}Ar$ ages for the SHV volcanic activity in the south of the island, which extend back to 290 ± 16 ka (Harford et al., 2002) with eruptions dated at c. 180 ka, c. 150 ka, c. 135 ka, c. 40 ka, and c. 25 ka. Peaks in the zircon age probability density function distribution at c. 45 ka and c. 150 ka (Fig. 6) agree with some of the $^{40}Ar/^{39}Ar$ dated eruptive events. Significantly, zircon crystallisation continued between eruptions indicating the presence of melt at depth through periods of eruptive quiescence.

However, the zircon ages contrast starkly with brief residence times derived from modelling of Sr diffusion in plagioclase, that is 15 to 320 y for the andesite of the 1995–2010 eruptions and up to only 1200 y for the older SHV rocks (Zellmer et al., 2003b). This reflects decoupling between long- and short-term magma storage conditions. Zellmer et al. (2003a) interpreted the short residence times for the major mineral plagioclase to result from diffusion in three dimensions during repeated intrusion and rapid crystallisation of small volumes of andesite magma into the upper crust. Subsequently, small intrusions were remobilised by hot mafic magma resulting in convective amalgamation of andesites of different ages with short upper crustal residence times (Zellmer et al., 2003a). This can be related to the episodic nature of the SHV eruptions, separated by long periods of quiescence. By contrast, secular equilibrium of whole-rock U-Th isotopes led these authors to extend the time between addition of the source slab-fluid signature to the magma and eruption to >350 ka. From this, prolonged magma crustal residence at depth was inferred. Reconciliation of different mineral residence timescales is only possible if, shortly before eruption, crystals with different histories, i.e., from different parts of the magmatic system were amalgamated in eruptible magma bodies. In fact, mismatch of accessory and major mineral residence times is common in other arc volcanoes because major mineral phases are more sensitive to reaction upon recharge than zircon (e.g., Cooper, 2015; Cisneros de León and Schmitt, 2019).

The SHV zircon ages reflect prolonged pre-eruptive crystal residence in a magma reservoir crystalline mush (cf., Cooper, 2015, and references therein; Szymanowski et al., 2017; Cisneros de León et al., 2019; Cisneros de León and Schmitt, 2019; amongst others). The crystalline mush was remobilised and amalgamated just prior to, or during eruption, because longer timescales related to mafic magma recharge eruption mush destabilisation would have resulted in complete resorption of the zircon (see Section 5.4 below). As a consequence of its small size zircon preferentially segregates into interstitial melt from remobilised crystal mushes compared to coeval major phases, highlighting again the potential for different phases in the same rock to record quite disparate histories (Claiborne et al., 2006b).

5.3. Insights into magmatic processes from zircon mineral chemistry: zircon crystallisation – melt volumes

5.3.1. Conditions of zircon crystallisation – composition

Uniform εHf combined with lack of correlation with age or Ti-in-zircon calculated crystallisation temperature (Figs. 10 and 14) suggest that the observed trace element heterogeneity arises from variability in melting and fractionation processes rather than reflecting variability in source composition or assimilation. A simple relationship between zircon trace element concentrations and degree of fractional crystallisation that would be expected for closed system evolution of a uniform melt is not evident in the SHV dataset. Arrays of zircon grains dominated by fractional crystallisation show negative correlations between zircon-compatible elements, for example, U, Th, Y and REE, and both Ti-in-zircon crystallisation temperatures and the differentiation index Zr/Hf (e.g., Storm et al., 2012a; Troch et al., 2018; Cisneros de León and Schmitt, 2019). The SHV zircon shows no correlation between these elements and Zr/Hf although several correlate, but positively, with calculated Ti-in-zircon crystallisation temperatures (Figs. 9 and 14). Uranium, Th, Nb, Ta and REE, – as well as Sr and Eu/Eu*, related to plagioclase fractionation – display a moderate positive correlation with Ti-in-zircon crystallisation temperature. This indicates the elements were preferentially incorporated into zircon that crystallised at higher temperatures, i.e., they are presumably early-formed. Progressive zircon crystallisation depleted the melt in these elements, so that at lower temperature concentrations are reduced. In contrast, Hf behaviour is decoupled from the other zircon-compatible trace elements, Zr/Hf correlates negatively with fractionation index Eu/Eu* and Ti-in-zircon crystallisation temperature (Fig. 14). Furthermore, the low SHV zircon Zr/Hf indicates, at least localised, extensive fractionation relative to the host andesite, which is consistent with the presence of interstitial rhyolitic groundmass glass (Christopher et al., 2014).

We suggest that the lack of typical fractionation-related correlations results from the SHV rocks preserving a heterogenous antecrystic collection of zircon. At a given value of Zr/Hf, that is a set level of fractionation, U for example, varies up to fourfold. Distinctive individual fractionation trends could be present in the dataset but masked by superposition of numerous parallel or subparallel trends from various initial melt compositions resulting in an apparent lack of correlation. The range of starting compositions may be conditioned by the degree of melt in isolated melt lenses where zircon became locally saturated.

Notwithstanding possible cryptic correlations, we propose that zircon U and Th abundances, and those of similar trace elements, reflect the crystallinity of the melt volume from which it formed (cf., Miller and Wooden, 2004; Storm et al., 2012a). Storm et al. (2012a) highlighted the conclusion of Miller and Wooden (2004) that if the compositional effect of extensive fractionation of phenocryst phases such as plagioclase dominated over zircon crystallisation, residual melt Th and U enrichment would ensue. The same effect could result, of course, from very low degrees of partial melting. Local variations in crystallinity can explain variable U and Th abundances without systematic co-variation with Zr/Hf, such as in the SHV zircon. Taking a typical partition coefficient for U in zircon of 126 (Charlier and Zellmer, 2000; Blundy and Wood, 2003) the measured range of zircon U = 37–196 ppm would be in equilibrium with melts with U = 0.2–1.5 ppm. The whole-rock U measured in the andesites and enclaves ranges from ~0.7–0.85 ppm and ~ 0.3–0.7 ppm, respectively. So, the lower zircon U concentrations are in equilibrium with whole-rock compositions. Yet, the highest values would require ~50% crystallisation, if, as is reasonable to assume, U is incompatible in the major mineral phases and zircon comprises a very small, <<1%, modal proportion of the fractionating assemblage. Therefore, the system would be rheologically quite rigid, at the limit of eruptiblity. If zircon grew in a such high crystallinity-low fraction melt, U and Th concentrations would be relatively high and variable, with the amount of zircon that could form limited by the melt Zr content. Both U and Th show strong positive correlations with REE suggesting the concentrations of these elements were also controlled by melt fraction (Fig. 15). That all these elements also correlate positively with calculated Ti-in-zircon crystallisation temperatures (Fig. 14) indicates higher concentrations in hotter melts. Seemingly, zircon crystallised from Zr-saturated melts that had relatively high concentrations of U, Th, REE and also Ti. This scenario is considered in more detail in the next section.

5.3.2. Conditions of zircon crystallisation – temperature

Calculated SHV Ti-in-zircon crystallisation temperatures vary by ~100°C in a single thin section: 680°C to 785°C, andesites 710–785°C, contact 695–770°C, and enclaves 680–770°C, evidencing a complex thermally heterogeneous system. It is noteworthy that the lower limit is also the temperature of the water-saturated rhyolite solidus, 680°C, at upper crustal pressures (Holtz and Johannes, 2014). Most of the crystallisation temperatures are appreciably higher than the whole-rock zircon saturation temperatures (ZST) indicating andesite and enclave compositions are zircon undersaturated. The melt in which the zircon grew was more Zr-rich than the host andesites or enclaves, consistent with the majority of the zircon crystals being antecrysts.

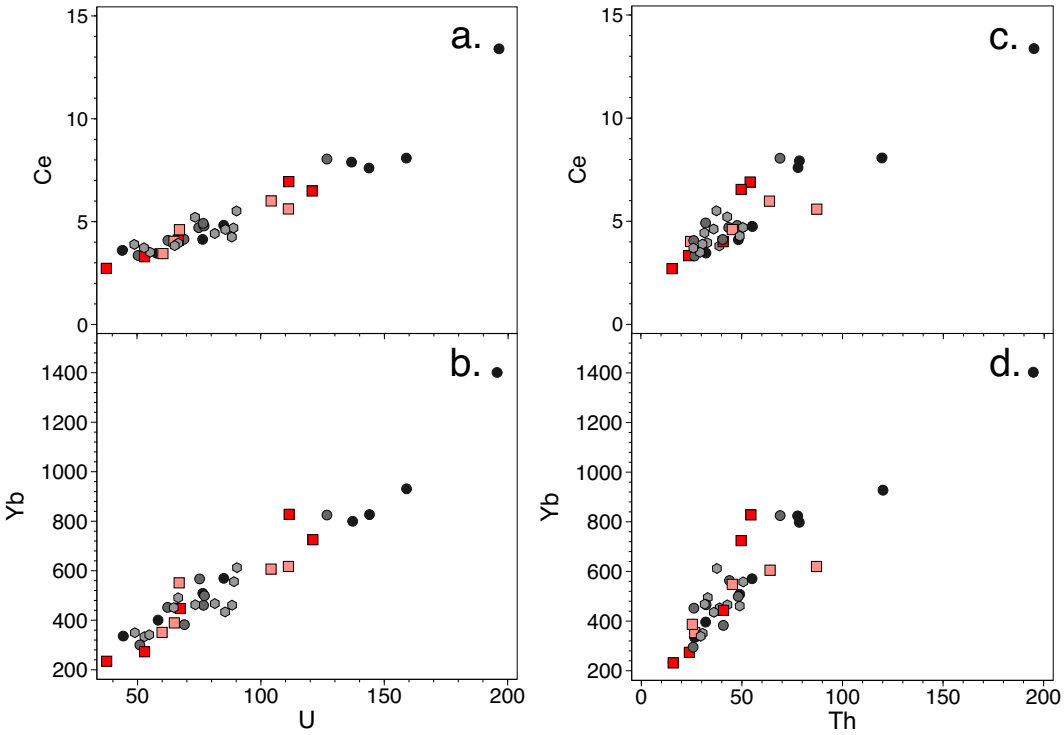

Fig. 15. Plots of rare earth elements versus U and Th: a. Ce versus U; b. Yb versus U; c. Ce versus Th; d. Yb versus Th. Both U and Th show strong positive correlations with the REE. All elements expressed in ppm.

Uncommonly high Ti-in-zircon crystallisation temperatures, relative to zircon saturation temperatures, could be the result of zircon growth in pockets of Zr-rich melt that formed as cumulate mush melted during reheating (Claiborne et al., 2010); or alternatively reflect disaggregated crystals from elevated temperature mafic magma that had fractionated. Absence of multiple resorption surfaces in the SHV zircon grains argues against the first scenario, as does the zircon-undersaturated nature of the host andesite and enclave magma because increasing the temperature of such compositions would not result in zircon crystallisation. In addition, although the SHV zircon crystallisation was protracted, no clear systematic temperature variation with age nor punctual higher temperature events were detected as might be expected if the magmatic system crystallising zircon was affected by significant intrusion of hotter more basic magma over time (cf., Claiborne et al., 2010; Cisneros de León and Schmitt, 2019). The more probable scenario for SHV is of repeated episodes of crystallisation in separate melt lenses – as corroborated by the range of SHV ages. The relatively high SHV Ti-in-zircon crystallisation temperatures are, therefore, consistent with our suggestion, based on heterogeneous zircon-compatible trace element concentrations, of zircon formation in small, interstitial, variably evolved melt lenses within the magma reservoir.

An additional effect in the context of small melt lenses is that the concentration of slow diffusing elements, including Zr, near fast growing crystals such as Fe-Ti oxide or other phenocrysts can lead to local supersaturation (Bacon, 1989). Significantly, as noted above, in the andesites zircon is commonly present as inclusions in amphibole phenocrysts or in the groundmass adjacent to Fe-Ti oxide phenocrysts. The diffusion effect may also impact on the behaviour of Ti and, as a consequence, calculated Ti-in-zircon crystallisation temperatures. Overestimation of these temperatures may occur in unusual, extremely fractionated, lower-temperature conditions which alters Ti partitioning into zircon (Troch et al., 2018). Also, in locally Zr-supersaturated melt lenses, diffusion of Ti into oxide phases may change the Ti activity values from those calculated using equilibrium magnetite-ilmenite pair compositions. This would affect Ti-in-zircon crystallisation temperatures: higher $aTiO_2$ would lower the calculated temperature; lower $aTiO_2$ would raise it. This process could explain the unanticipated positive correlation between what are unexpectedly high temperatures and U, Th and the REE. In heterogeneous mush systems it is plausible, therefore, that Ti-in-zircon crystallisation temperatures reflect conditions in small-scale melt lenses rather than magma-wide conditions.

5.3.3. Conditions of zircon crystallisation – oxidation

In addition to temperature and degree of crystallisation, magma oxygen fugacity also plays a role in zircon-melt element partitioning. Zircon often has both elevated Ce – indicating oxidising conditions – and depleted Eu – indicating reducing conditions – which shows that factors other than just oxygen fugacity control the distribution of these elements. Melt Ce content is not affected by crystallisation of any major mineral whereas Eu may be depleted by plagioclase crystallisation and enriched by apatite crystallisation (Trail et al., 2012). For this reason, Ce anomalies are usually considered to be a more reliable qualitative indicator of natural melts oxidation state.

The SHV zircon positive Ce/Ce* anomalies do not correlate with the degree of fractionation, e.g., indicated by Zr/Hf (Fig. 9). The Eu/Eu* anomalies, on the other hand, do as expected given the dependence on plagioclase fractionation (Fig. 9), with the largest negative anomalies in zircon being recorded in the most evolved rocks. Notably, the absence of La enrichment relative to Pr implies that zircon crystallised prior to, or in the absence of, other LREE-bearing accessory minerals such as monazite (Trail et al., 2012). This is significant because extensive crystallisation of monazite that preferentially includes Ce^{3+} relative to Ce^{4+} could lead to a positive Ce anomaly in the melt and a corresponding negative anomaly in the monazite in particularly oxidising conditions. In this scenario zircon Ce anomalies would not simply reflect the oxidation state of natural melts but instead overestimate it. As it is, the SHV range of Ce anomalies indicates zircon crystallised under variably oxidising conditions as a result of differences in magma volatile content (e.g., Kelley and Cottrell, 2009). Accordingly, calculation of fO_2 values using our SHV zircon trace element data and the calibrations of Smythe and Brenan (2016) and Loucks et al.

(2020) give a comparatively wide range of values relative to the FMQ buffer: + 0.4 to −1 and + 1.5 to − 1, respectively. This compares with Fe-Ti oxide pair fO_2 values of +1.96 to +1 FMQ buffer (Christopher et al., 2014). However, as noted above zircon growth close to Fe-Ti oxide phenocrysts may change the behaviour of Ti partitioning and so calculated Ti-in-zircon crystallisation temperatures. This would affect temperature-dependent comparison with a given oxygen fugacity buffer. The negative fO_2 values suggest comparison temperatures are too high, consistent with the possibility of bias towards elevated temperatures discussed in the previous section. Nevertheless, regardless of exact values, variation in oxygen fugacity values is consequential for three reasons. Firstly, it indicates heterogeneity in the magma during crystallisation. Secondly, it can condition zircon partition coefficients and redox-sensitive trace element behaviour during melting and crystallisation. Thirdly, an oxidised nature of hydrous magmas may be related to melt-mantle H_2 reactions (Tollan and Hermann, 2019). Volatiles are the primary driving force for volcanic eruptions (Cashman, 2004), and degassing behaviour and magma ascent rate can condition eruptive style, i.e., rapid – explosive versus slow – effusive; the SHV eruptive style has important implications for associated hazard and risk on Montserrat (e.g., Hicks and Few, 2015).

5.3.4. Conditions of zircon crystallisation – summing up

We suggest zircon crystallised in evolved dacitic-rhyolitic interstitial melt pockets, or localised patches of Zr-saturated melt near fast growing phenocrysts, in the andesite mush and then mingled into the enclaves. Preservation of zircon in the least-evolved enclave contacts resulted when the hotter mafic magma quenched as it came into contact with the cooler andesite.

Regarding melt distribution in the magma reservoir, recent modelling by Paulatto et al. (2019) inverted gravity anomalies and active-source P-wave travel times to develop 3-D models of density and P-wave velocity down to 8 km to constrain melt geometry, fraction, and temperature. This led them to increase estimates of melt fractions from on average ~ 6% to 17%. The maximum predicted melt fraction, 35%, was modelled at 5–6 km, the top of a partial melt region that extended down to 8 km. This, they concluded, comprised relatively small, grain-scale to 100-m-scale, sills and dykes of eruptible lenses within a transcrustal mush. The low degree of melting fits with the volumetrically-restricted melt lenses inferred from the zircon compositions in this work.

Considering the zircon mineral chemistry data in the context of a transcrustal magma reservoir, variable, crystallisation temperatures >750°C are frequently recorded over timescales >100 ky. However, the proportion of the magma reservoir at that temperature is not constrained nor the longevity of the putative heterogeneous melt lenses. What is more, independent of when the zircon crystallised, and at what temperature, the new age data demonstrate it was subsequently stored at a lower temperature below mush lock up, ~50% crystal fraction, near or below the solidus, for many thousands of years. At some point, between crystallisation and eruption, the preserved zircon was amalgamated in the andesite, and enclaves, most probably during mafic magma recharge mush destabilisation (cf., Cashman et al., 2017).

Irrespective of the details of the thermochemical conditions and processes of zircon crystallisation the key point, as was the case for the geochronological data age range, is the compositional heterogeneity observed at thin section scale. Together, these data evidence the magmatic system had a complex history involving amalgamation of temporally and spatially distinct zircon from an intermediate-acid transcrustal magma reservoir with limited interconnectivity, into an eruptible 'crystal cargo' that also included major mineral phases. This inherent heterogeneity was further complicated by recharge of the system by mafic magma, the ascent of which may have been facilitated by brittle behaviour of the high crystallinity andesite mush. The observed andesite subanhedral, partially corroded and resorbed zircon that lack overgrowth rims may have resulted from the last significant mingling with hot zircon-undersaturated enclave mafic magma as discussed below.

5.4. Insights into magmatic processes from zircon textures and preservation: magma mingling – timing of eruption triggering

Zircon morphology and size depends on whether it saturated early or late in the magmatic crystallisation sequence (Hoskins and Schaltegger, 2003). Early formed crystals are typically euhedral and relatively large with 1:2–1:4 width-length ratios (Corfu et al., 2003). Late-formed crystals are often anhedral as they grow in interstices between other minerals, e.g., in plutonic magmas. Fast-growing crystals in volcanic magmas are commonly prismatic to acicular with up to 1:12 width-length ratios. Even so, it should be borne in mind that zircon morphologies and sizes can vary considerably in a single age population from the same rock; zircon from different rocks can have similar characteristics with no petrogenetic association; and zircon external morphology can change during a single or multiple growth events.

The SHV zircon was preferentially preserved, as euhedral-subhedral grains, in or near the least-evolved enclave-andesite quenched contacts. It is found more rarely as subhedral-anhedral grains in the associated host andesite where they are often corroded (Figs. 3 and 5). No clear zircon morphological differences were detected in the most-evolved enclave-andesite pair. Plail et al. (2018) deduced that differences in the enclave borders provide information about how the magmas interacted. They explained the formation of the enclaves as the result of syn-eruptive mafic underplating of an andesite magma reservoir followed by magma mixing that gave rise to a thermal boundary layer between the two magmas. Formation of quenched contacts in the least-evolved compositions was attributed to rapid thermal re-equilibration of the mafic magma as it intruded the andesite directly, perhaps as a plume. The diffuse margins in the most-evolved samples, on the other hand, were interpreted to preserve vesiculation-driven interaction of the andesite and magma from a slowly cooled mafic-intermediate hybridised layer that was more prone to mingle.

Several studies have reported petrographic and mineral chemistry evidence for transfer of material and volatiles between the enclaves and the andesite. Mixing of phenocrysts, including variably oxidised amphibole, reversely zoned plagioclase and clinopyroxene rimmed orthopyroxene is evident in SHV rocks. This resulted from non-uniform reheating and remobilisation of a relatively old, cool, ~850°C, and crystal-rich andesite magma by variable interaction with an intruding mafic magma (Murphy et al., 2000; Humphreys et al., 2009a). Disaggregation of the mafic magma into the andesite has been attributed to shear-stress (Humphreys et al., 2009a) or decompression exsolution of crystals and volatiles (Edmonds et al., 2014). Up to 6 vol% of 'cryptic' disaggregated mafic material (Humphreys et al., 2013) has been recorded in the andesites in addition to the 1–12 vol% of enclaves (Murphy et al., 2000; Barclay et al., 2010; Komorowski et al., 2010; Mann et al., 2013; Plail et al., 2014). Remarkably, up to 15–25 vol% of 'inherited' andesite phenocrysts and late-stage rhyolitic melt are also found in the most-evolved diffuse contact enclaves, and more rarely in the primitive enclaves (Murphy et al., 2000; Zellmer et al., 2003a; Barclay et al., 2010; Humphreys et al., 2009a, 2009b; Plail et al., 2014; Humphreys et al., 2013; Christopher et al., 2014; Plail et al., 2018). The zircon results, however, suggest that rather than considering bulk percentages, individual enclaves need to be considered in detail to unravel mingling processes – to paraphrase H. H. Read 'there are enclaves and enclaves'.

Injection of hot primitive magma into an intermediate mush would cause crystal resorption near the magma mingling contact and, further away, heating and remobilisation (Cisneros de León and Schmitt, 2019). Latent heat of ensuing crystallisation would partially melt more distal regions of the host mush, adding intermediate magma, including zircon, to the mix. This would promote new zircon crystallisation as a result of local Zr saturation around xenocrystic zircon (Cisneros de León and Schmitt, 2019). Such a process could have been important in older recharge cycles in the SHV magmatic system – although it should be noted that overgrowth rims are not observed. It cannot, however,

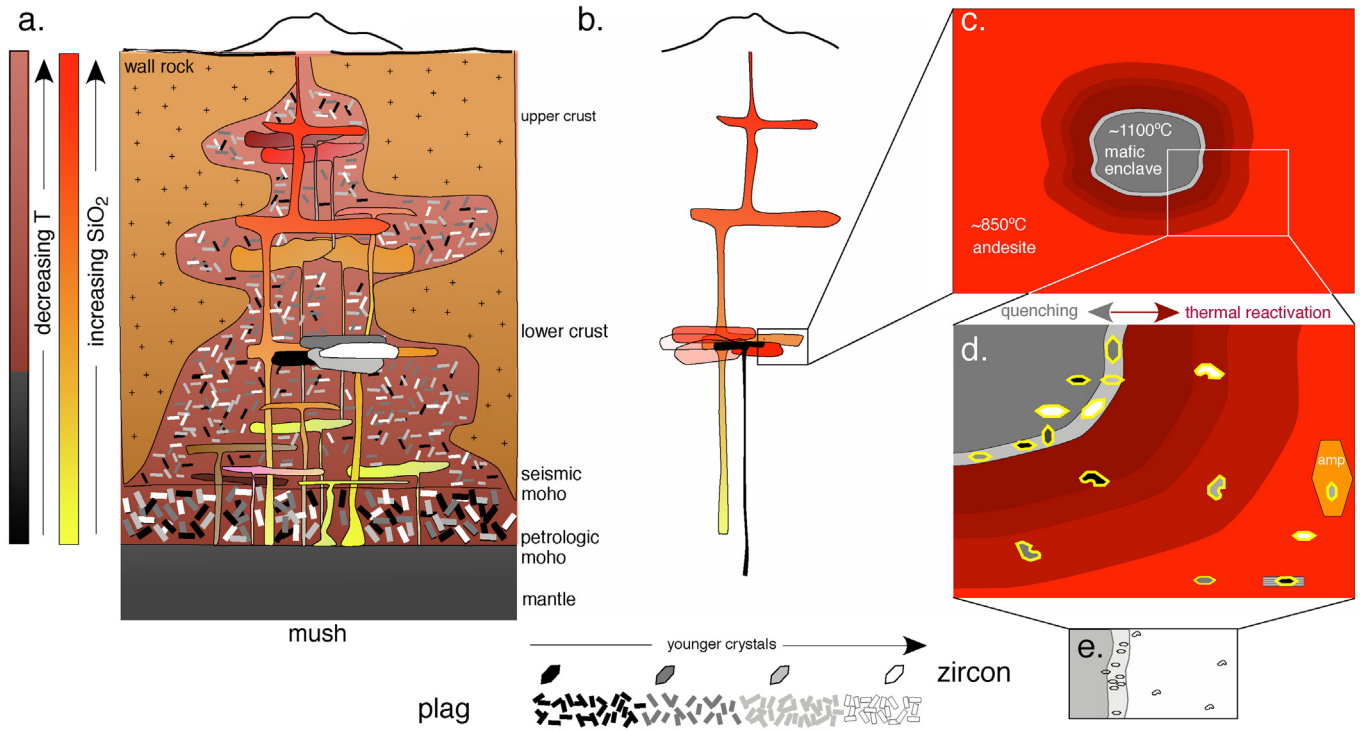

Fig. 16. Schematic representation of processes beneath the Soufrière Hills Volcano: a. transcrustal magma reservoir, note the decreasing temperature, increasing SiO_2 and variation in age of crystals in the mush (modified from Cashman et al., 2017); b. melt lenses of the transcrustal magma reservoir, the black lens represents injection of mafic magma; c. detail of the mafic and andesite magma interaction, temperatures from Humphreys et al. (2009a); d. preferential preservation of zircon crystals in the quenched contact between the mafic magma enclave and the andesite, pale grey, and corrosion of the zircon by thermal reactivation in the andesite where not shielded in phenocryst phases (amp – amphibole); e. example of zircon preservation in the quenched contact between the mafic enclave and andesite as seen in thin section, as shown in Fig. 3.

explain growth of zircon in the mingled phase V dome collapse blocks and their enclave-andesite quenched contacts studied here. This is because the zircon is not newly formed since recent phase III, mid-2005 to early-2007, mafic magma injection because crystals range in age from c. 40–160 ka. In any case, zircon could not have grown between mingling and eruption because growth rates are too slow, a ~ 50 μm zircon will not form in under 100 years in a metaluminous melt (e.g., Watson, 1996). Furthermore, as noted above, enclave and andesite zircon saturation temperatures, 550–650°C, are lower than Ti-in-zircon crystallisation temperatures, ~680–785°C. This indicates those magmas were zircon undersaturated so the zircon is antecrystic – crystals from the same magma system but not related to the host liquid – not autocrystic, i.e., not syn-magmatic (cf., Siégel et al., 2018). Nevertheless, local Zr saturation could have enhanced the preferential zircon preservation in the enclave-andesite quenched contact.

As zircon is generally considered to be both chemically and physically resilient, its heterogeneous preservation is somewhat mysterious: euhedral-subhedral grains in the quenched enclave-andesite contacts and near to these in the enclaves and as subhedral-anhedral corroded grains in the andesite (Fig. 5). At first sight, this appears counter-intuitive because, given the relative SiO_2 content of the enclave and andesite, 50.5 wt% and 58.5 wt% respectively, zircon should crystallise in the andesite – or more likely, a more evolved pre-mingling composition such as dacite-rhyolite. Whole-rock data show zircon was not fractionating from the enclaves nor andesite because Zr shows a clear, continuous, inflexion-free, positive correlation up to 62 wt% SiO_2 (Christopher et al., 2014, their Fig. 17.9). As mentioned above, an exception is minor zircon that crystallised in evolved late-stage melt pockets or near rapidly growing phenocrysts where, as a result of slow Zr diffusion, melts become locally supersaturated in zircon (Bacon, 1989). What is more, the pre-eruptive temperature of the enclave magma was hot ~1050–1100°C (Humphreys et al., 2009a) and volatile rich >8 wt% H_2O (Edmonds et al., 2014), whereas the temperature of the pre-eruptive andesite magma was cooler ~850°C (Couch et al., 2003) with 6–9 wt% H_2O (Edmonds et al., 2016). Considering kinetics of zircon dissolution, however, can shed light upon the preservation paradox – depending, as it does, on time, temperature and melt undersaturation with respect to zircon (Watson, 1996). These factors are controlled to a great extent by the intensity and duration of a magmatic event and melt reservoir volume. For example, numerical modelling suggests even the largest Montserrat zircon grains, ~200 μm, would dissolve in a 1100°C mafic melt in a few weeks (Watson, 1996). Hence, the only way zircon could have survived in the mafic melt is if i. dissolution was inhibited by rapid cooling, or ii. they were shielded from the magma as inclusions in a major mineral either prior to mingling or after mingling and before dissolution (Bea et al., 2007; Bea and Montero, 2013).

The SHV zircon range of ages and compositions is compatible with mush destabilisation that can result in eruptive magma batches, preserved as single rock samples, composed of minerals with very different crystallisation histories as summarized in Fig. 16. Intrusion of the heterogeneous SHV crystal-rich andesite mush by hot volatile mafic magma led to initiation of mingling that was quickly arrested as the mafic material quenched, releasing heat and volatiles as it solidified. At the contact between the two magmas zircon was trapped, shielded, and so preserved during this rapid solidification. Zircon mingled into the enclaves but was dissolved preferentially to other mineral phases because of the higher temperature and, most importantly, because of the zircon-undersaturated composition of the mafic magma. In the andesite, mafic magma intrusion led to concomitant thermal reactivation and corrosion of zircon. No such thermal-preservation effect was produced in the lower temperature more hybrid, most-evolved, enclaves that preserve fewer zircon crystals. Zircon is generally absent in the erupted andesites and where found are most commonly shielded inclusions in amphibole phenocrysts or in the groundmass adjacent to Fe-Ti oxide phenocrysts. Had the 2010 dome collapse not exposed and effectively frozen the sub-volcanic magma reservoir, the zircon-rich

quenched contacts may not have been revealed, and zircon dissolution in the andesite may have progressed to completion.

6. Conclusions

Our new zircon data place constraints on processes in the Soufrière Hills Volcano sub-volcanic magma reservoir.

i. Zircon ^{238}U-^{230}Th disequilibrium ages record that at least some part of the SHV magma system was zircon-saturated over the last 250 ky and reflect prolonged pre-eruptive crystal residence in a transcrustal mush. Comparison with SHV $^{40}Ar/^{39}Ar$ ages reveals zircon crystallisation continued between eruptions indicating the presence of melt at depth through periods of eruptive quiescence.

ii. Zircon mineral chemistry records crystallisation from compositionally and thermally heterogeneous melts in small isolated lenses where the melt becomes locally zircon saturated. Hafnium isotope data show that these melts all had a very similar, typical island arc, source composition.

iii. The range of zircon ages and compositions at thin section scale reveals amalgamation of crystals, that formed in distinct melt lenses, from different parts of the magmatic mush system at some point just prior to eruption most probably related to mafic magma recharge mush destabilisation.

iv. Injection of mafic magma added heat and volatiles to the andesitic melt-mush system significantly perturbing zircon preservation. Based on morphology it appears that zircon was preferentially shielded in or near the quenched contacts of the least-evolved mafic enclaves whereas it was corroded in the thermally reactivated host andesite mush.

v. The age and mineral chemistry of zircon from recent volcanic rocks has huge potential to place temporal and compositional constraints on processes in active sub-volcanic magma systems over both long and short time and length scales.

Information obtained about the physical and thermal state of magma storage conditions and the processes and timescales needed to mobilise magmas before eruption can be fed into medium-long term hazard mitigation planning strategies. Here we place constraints on absolute timescales of crystal and melt storage, melt volumes and relative timing of eruption triggering. Real-time monitoring data, for example, geodesy and gas emission measurements, indicate current unrest of Soufrière Hills Volcano magmatic system (Odbert et al., 2014; Nicholson et al., 2013). Implications in terms of future eruptions include potential danger to aviation, infrastructure damage, harm to agriculture and safety, health and well-being for local populations and neighbouring regions.

Declaration of Competing Interest

The authors declare that they have no known competing financial interests or personal relationships that could have appeared to influence the work reported in this paper.

Acknowledgements

This project has received funding from the European Union's Horizon 2020 research and innovation programme under the Marie Skłodowska-Curie grant agreement No. 749611 (JHS). We also acknowledge funding from the Natural Environment Research Council Isotope Geoscience Facilities Steering Committee, grant IP-1746-1117 (JB). The work has been financially supported by the Spanish grant CGL 2017-84469-P (JHS). Funding for open access charge: Universidad de Granada/CBUA. Alexander Varychev at the University of Heidelberg, Germany, and Jeremy Rushton at the British Geological Survey, U.K., are thanked for help with analytical work. José Luis Macias is thanked for editorial handling. We are obliged to two anonymous reviewers for the time and effort they took to help us improve the clarity and rigour of our interpretations.

Appendix A. Supplementary data

Supplementary data to this article can be found online at https://doi.org/10.1016/j.jvolgeores.2021.107390.

References

Bacon, C.R., 1989. Crystallization of accessory phases in magmas by local saturation adjacent to phenocrysts. Geochim. Cosmochim. Acta 53, 1055–1066.
Barboni, M., Boehnke, P., Schmitt, A.K., Harrison, T.M., Shane, P., Bouvier, A.S., Baumgartner, L., 2016. Warm storage for arc magmas. Proc. Natl. Acad. Sci. U. S. A. 113, 13959–13964.
Barclay, J., Herd, R.A., Edwards, B.R., Christopher, T., Kiddle, E.J., Plail, M., Donovan, A., 2010. Caught in the act: implications for the increasing abundance of mafic enclaves during the recent eruptive episodes of the Soufrière Hills Volcano, Montserrat. Geophys. Res. Lett. 37, 1–5.
Bea, F., Montero, P., 2013. Diffusion-induced disturbances of the U-Pb isotope system in pre-magmatic zircon and their influence on SIMS dating. A numerical study. Chem. Geol. 349, 1–17.
Bea, F., Montero, P., González-Lodeiro, F., Talavera, C., 2007. Zircon inheritance reveals exceptionally fast crustal magma generation processes in Central Iberia during the Cambro-Ordovician. J. Petrol. 48, 2327–2339.
Blundy, J., Wood, B., 2003. Partitioning of trace elements between crystals and melts. Earth Planet. Sci. Lett. 210, 383–397.
Boehnke, P., Watson, E.B., Trail, D., Harrison, T.M., Schmitt, A.K., 2013. Zircon saturation re-revisited. Chem. Geol. 351, 324–334.
Bouysse, P., Westercamp, D., 1990. Subduction of Atlantic aseismic ridges and Late Cenozoic evolution of the Lesser Antilles island arc. Tectonophysics 175, 349–355.
Breitkreuz, C., Schmitt, A.K., Repstock, A., Kause, J., Schulz, B., Bergmann, F., Bischoff, J., Le Friant, A., Ishizuka, O., 2021. Record and provenance of Pleistocene volcaniclastic turbidites from the central Lesser Antilles (IODP EXpedition 340, Site U1398B). Mar. Geol. 438 e106536.
Cashman, K.V., 2004. Volatile controls on magma ascent and eruption. In: Sparks, R.S.J., Hawkesworth, C.J. (Eds.), The State of the Planet: Frontiers and Challenges in Geophysics. 150, pp. 109–124 Geophysical Monograph Series.
Cashman, K.V., Sparks, R.S.J., Blundy, J.D., 2017. Vertically extensive and unstable magmatic systems: a unified view of igneous processes. Science 355, 1280–1289.
Cassidy, M., Taylor, R.N., Palmer, M.R., Cooper, R.J., Stenlake, C., Trofimovs, J., 2012. Tracking the magmatic evolution of island arc volcanism: insights from a high-precision Pb isotope record of Montserrat, Lesser Antilles. Geochem. Geophys. Geosyst. https://doi.org/10.1029/2012GC004064.
Charlier, B., Zellmer, G.F., 2000. Some remarks on U–Th mineral ages from igneous rocks with prolonged crystallisation histories. Earth Planet. Sci. Lett. 183, 457–469.
Christopher, T.E., Humphreys, M.C.S., Barclay, J., Genareau, K., De Angelis, S.M.H., Plail, M., Donovan, A., 2014. Chapter 17 Petrological and geochemical variation during the Soufrière Hills eruption, 1995 to 2010. In: Wadge, G., Robertson, R.E.A., Voight, B. (Eds.), The Eruption of Soufrière Hills Volcano, Montserrat from 2000 to 2010. 39. Geological Society, London, pp. 317–342 Memoirs.
Christopher, T.E., Blundy, J., Cashman, K., Cole, P., Edmonds, M., Sparks, Smith P.-J., R.S.J., and Stinton A., 2015. Crustal-scale degassing due to magma system destabilization and magma-gas decoupling at Soufrière Hills Volcano, Montserrat. Geochem. Geophys. Geosyst. https://doi.org/10.1002/2015GC005791.
Cisneros de León, A., Schmitt, A.K., 2019. Intrusive reawakening of El Chichón volcano prior to its Holocene eruptive hyperactivity. J. Volcanol. Geotherm. Res. 377, 53–68.
Cisneros de León, A., Schmitt, A.K., Storm, S., Weber, B., Schindlbeck-Belo, J.C., Trumbull, R.B., Juárez, F., 2019. Millennial to decadal magma evolution in an arc volcano from zircon and tephra of the 2016 Santiaguito eruption (Guatemala). Lithos 340–341, 209–222.
Claiborne, L.L., Miller, C.F., Walker, B.A., Wooden, J.L., Mazdab, F.K., Bea, F., 2006a. Tracking magmatic processes through Zr/Hf ratios in rocks and Hf and Ti zoning in zircons: an example from the Spirit Mountain batholith, Nevada. Min. Mag. 70, 517–543.
Claiborne, L.L., Furbish, D.J., Miller, C.F., 2006b. Determining mechanics of segregating small crystals from melt using modeling and SHRIMP-RG trace element analysis of zircons: an example from the Spirit Mountain Batholith, Nevada. EOS Trans. Am. Geophys. Union 87 V54B–02.
Claiborne, L.L., Miller, C.F., Flanagan, D.M., Clynne, M.A., Wooden, J.L., 2010. Zircon reveals protracted magma storage and recycling beneath Mount St. Helens. Geology 38, 1011–1014.
Cooper, K.M., 2015. Timescales of Crustal Magma Reservoir Processes: Insights from U-Series Crystal Ages. Geological Society, London, pp. 141–174 Special Publication 422.
Cooper, K.M., 2019. Time scales and temperatures of crystal storage in magma reservoirs: implications for magma reservoir dynamics. Phil. Trans. R. Soc. A 377, 20180009. https://doi.org/10.1098/rsta.2018.0009.
Corfu, F., Hoskins, Hanchar J.M., P.W.O.and Kinny P., 2003. Atlas of zircon textures. In: Hanchar, J.M., Hoskins, P.W.O. (Eds.), Zircon. Reviews in Mineralogy and Geochemistry53, pp. 469–500.
Couch, S., Harford, C.L., Sparks, R.S.J., Carroll, M.R., 2003. Experimental constraints on the conditions of formation of highly calcic plagioclase microlites at the Soufrire Hills Volcano, Montserrat. J. Petrol. 44, 1455–1475.
Coussens, M., Cassidy, M., Watt, S.F.L., Jutzeler, M., Talling, P.J., Barfod, D., Gernon, T.M., Taylor, R., Hatter, S.J., Palmer, M.R., Montserrat Volcano Observatory, 2017. Long-term changes in explosive and effusive behaviour at andesitic arc volcanoes: chronostratigraphy of the Centre Hills Volcano, Montserrat. J. Volcanol. Geotherm. Res. 333, 15–35.

Dhuime, B., Hawkesworth, C.J., Cawood, P., 2011. When continents formed. Science 331, 154–155.

Edmonds, M., Humphreys, M.C.S., Hauri, E.H., Herd, R.A., Wadge, G., Rawson, H., Ledden, R., Plail, M., Barclay, J., Aiuppa, A., Christopher, T.E., Giudice, G., Guida, R., 2014. Chapter 16. Pre-eruptive vapour and its role in controlling eruption style and longevity at Soufrière Hills Volcano. In: Wadge, G., Robertson, R.E.A., Voight, B. (Eds.), The Eruption of Soufrière Hills Volcano, Montserrat from 2000 to 2010. Geological Society, London, pp. 291–315 Memoir 39.

Edmonds, M., Kohn, S.C., Hauri, E.H., Humphreys, M.C.S., Cassidy, M., 2016. Extensive, water-rich magma reservoir beneath southern Montserrat. Lithos 253, 216–233.

Edmonds, M., Cashman, K.V., Holness, M., Jackson, M., 2019. Architecture and dynamics of magma reservoirs. Phil. Trans. R. Soc. A 377, 20180298. https://doi.org/10.1098/rsta.2018.0298.

Ferry, J.M., Watson, E.B., 2007. New thermodynamic models and revised calibrations for the Ti-in-zircon and Zr-in-rutile thermometers. Contrib. Mineral. Petrol. 154, 429–437.

Ghiorso, M.S., Gualda, G.A., 2013. A method for estimating the activity of titania in magmatic liquids from the compositions of coexisting rhombohedral and cubic iron– titanium oxides. Contrib. Mineral. Petrol. 165, 73–81.

Grimes, C.B., Wooden, J.L., Cheadle, M.J., John, B.E., 2015. "Fingerprinting" tectonomagmatic provenance using trace elements in igneous zircon. Contrib. Mineral. Petrol. 170, 1–26.

Harford, C.L., Pringle, M.S., Sparks, R.S.J., Young, S.R., 2002. The volcanic evolution of Montserrat using $^{40}Ar/^{39}Ar$ geochronology. In: Druitt, T.H., Kokelaar, B.P. (Eds.), The eruption of Soufrière Hills Volcano, Montserrat, from 1995-1999. 21. Geological Society, London, pp. 93–113 Memoirs.

Harrison, T.M., Watson, E.B., Aikman, A.B., 2007. Temperature spectra of zircon crystallization in plutonic rocks. Geology 35, 635–638.

Hatter, S.J., Palmer, M.R., Gernon, T.M., Taylor, R.N., Cole, P.D., Barfod, D.N., Coussens, M., 2018. The evolution of the Silver Hills Volcanic Center, and revised $^{40}Ar/^{39}Ar$ geochronology of Montserrat, Lesser Antilles, with implications for island arc volcanism. Geochem. Geophys. Geosyst. https://doi.org/10.1002/2017GC007053.

Hicks, A., Few, R., 2015. Trajectories of social vulnerability during the Soufrière Hills volcanic crisis. J. Appl. Volcanol. 4, 10–24.

Holtz, F., Johannes, W., 2014. Maximum and minimum water contents of granitic melts: implications for chemical and physical properties ascending magmas. Lithos 23, 149–159.

Hoskins, P.W.O., Schaltegger, U., 2003. The composition of zircon and igneous and metamorphic petrogenesis. In: Hanchar, J.M., Hoskins, P.W.O. (Eds.), Zircon. Rev. in Min. and Geochem.. 53, pp. 27–62

Howe, T.M., Schmitt, A.K., Lindsay, J.M., Shane, P., Stockli, D.F., 2015. Time scales of intra-oceanic arc magmatism from combined U-Th and (U-Th)/He zircon geochronology of Dominica, Lesser Antilles. 1. Howe T.M. Geochem. Geophys. Geosyst. https://doi.org/10.1002/2014GC005636.

Humphreys, M.C.S., Edmonds, M., Christopher, T., Hards, V., 2009a. Chlorine variations in the magma of Soufrière Hills Volcano, Montserrat: insights from Cl in hornblende and melt inclusions. Geochim. Cosmochim. Acta 73, 5693–5708.

Humphreys, M.C.S., Christopher, T., Hards, V., 2009b. Microlite transfer by disaggregation of mafic inclusions following magma mixing at Soufrière Hills volcano, Montserrat. Contrib. Mineral. Petrol. 157, 609–624.

Humphreys, M.C.S., Edmonds, M., Christopher, T., Hards, V., 2013. A new method to quantify the real supply of mafic components to a hybrid andesite. Contrib. Mineral. Petrol. 165, 191–215.

Kahl, M., Chakraborty, S., Costa, F., Pompilio, M., Luizzo, M., Vicario, M., 2013. Compositionally zoned crystals and real-time degassing data reveal changes in magma transfer dynamics during the 2006 summit eruptive episodes of Mt. Etna. Bull. Volcanol. 75, 1–14.

Kelley, K.A., Cottrell, E., 2009. Water and the oxidation state of subduction zone magmas. Science 325, 605–607.

Komorowski, J.-C., Legendre, Y., Christopher, T., Bernstein, M., Stewart, R., Joseph, E., Fournier, N., Chardot, L., Finizola, A., Wadge, G., Syers, R., Williams, C., Bass, V., 2010. Insights into processes and deposits of hazardous vulcanian explosions at Soufrière Hills Volcano during 2008 and 2009 (Montserrat, West Indies). Geophys. Res. Lett. 37, 1–6.

Loucks, R.R., Fiorentini, M.L., Henríquez, G.J., 2020. New magmatic oxybarometer using trace elements in zircon. J. Petrol. 60, 1–30.

Mann, C.P., Wallace, P.J., Stix, J., 2013. Phenocryst-hosted melt inclusions record stalling of magma during ascent in the conduit and upper magma reservoir prior to vulcanian explosions, Soufrière Hills volcano, Montserrat, West Indies. Bull. Volcanol. 75, 687–702.

McDonough, W.F., Sun, S.S., 1995. The composition of the Earth. Chem. Geol. 120, 223–253.

McGee, L., Reagan, M., Handley, H., Turner, S., Sparks, R.S.J., Berlo, K., Barclay, J., Turner, M., 2019. Volatile behaviour in the 1995-2010 eruption of the Soufrière Hills Volcano, Montserrat recorded by U-series disequilibria in mafic enclaves and andesite host. Earth Planet. Sci. Lett. 524, 1–11.

Miller, J.S., Wooden, J.L., 2004. Residence, resorption and recycling of zircons in Devils Kitchen rhyolite, Coso Volcanic Field, California. J. Petrol. 45, 2155–2170.

Murphy, M.D., Sparks, R.S.J., Barclay, J., Carroll, M.R., Brewer, T.S., 2000. Remobilization of andesite magma by intrusion of mafic magma at the Soufrière Hills volcano, Montserrat, West Indies. J. Petrol. 41, 21–42.

Neuberg, J., Pascal, K., 2020. The continuing inflation of montserrat – and the end of the intrusion. EGU General Assembly 2020, Online, 4–8 May 2020, EGU2020-19745 https://doi.org/10.5194/egusphere-egu2020-19745.

Nicholson, E.J., Mather, T.A., Pyle, D.M., Odbert, H.M., Christopher, T., 2013. Cyclical patterns in volcanic degassing revealed by SO2 flux timeseries analysis: an application to Soufrière Hills Volcano, Montserrat. Earth Planet. Sci. Lett. 375, 209–221.

Odbert, H.M., Ryan, G.A., Mattioli, G.S., Hautmann, S., Gottsmann, J., Fournier, N., Herd, R.A., 2014. Volcano geodesy at the Soufrière Hills Volcano, Montserrat: a review. In: Wadge, G., Robertson, R.E.A., Voight, B. (Eds.), The Eruption of Soufrière Hills Volcano, Montserrat from 2000 to 2010. Geological Society, London, pp. 195–217 Chapter 11. Memoir 39.

Pankhurst, M.J., Morgan, D.J., Thordarson, T., Loughlin, S.C., 2018. Magmatic crystal records in time, space, and process, causatively linked with volcanic unrest. Earth Planet. Sci. Lett. 493, 231–241.

Paulatto, M., Moorkamp, M., Hautmann, S., Hooft, E., Morgan, J.V., Sparks, R.S.J., 2019. Vertically extensive magma reservoir revealed from joint inversion and quantitative interpretation of seismic and gravity data. J. Geophys. Res. Solid Earth 124, 11170–11191.

Pettingill, H.S., Patchett, P.J., 1981. Lu-Hf total-rock age for the Amîtsoq gneisses, West Greenland. Earth Planet. Sci. Lett. 55, 150–156.

Plail, M., 2014. Geochemical and Petrological Investigation into the Magmatic System at Soufrière Hills Volcano, Montserrat. PhD thesis University of East Anglia, UK.

Plail, M., Barclay, J., Humphreys, M.C.S., Edmonds, M., Herd, R.A., Christopher, T.E., 2014. Chapter 18 Characterization of mafic enclaves in the erupted products of Soufrière Hills Volcano, Montserrat, 2009 to 2010. In: Wadge, G., Robertson, R.E.A., Voight, B. (Eds.), The Eruption of Soufrière Hills Volcano, Montserrat from 2000 to 2010. Geological Society, London, pp. 343–360 Memoir 39.

Plail, M., Edmonds, M., Woods, A.W., Barclay, J., Humphreys, M.C.S., Herd, R.A., Christopher, T., 2018. Mafic enclaves record syn-eruptive basalt intrusion and mixing. Earth Planet. Sci. Lett. 484, 30–40.

O'Neill, H.St.C., Powneby, M.I., 1993. Thermodynamic data from redox reactions at high temperatures. I. An experimental and theoretical assessment of the electrochemical method using stabilized zirconia electrolytes, with revised values for the Fe-"FeO", Co-CoO, Ni-NiO and Cu-Cu_2O oxygen buffers, and new data for the W-WO_2 buffer. Contrib. Mineral. Petrol. 114, 296–314.

Schmitt, A.K., 2011. Uranium series accessory crystal dating of magmatic processes. Ann. Rev. Earth Planet. Sci. Lett. 39, 321–349.

Sheldrake, T., Caricchi, L., Weber, G., 2020. Episodic volcanism recorded in coral skeletons. Geological Society, London Volcanic and Magmatic Studies Annual Meeting, Plymouth.

Siégel, C., Bryan, S.E., Allen, C.M., Gust, D.A., 2018. Use and abuse of zircon-based thermometers: a critical review and a T recommended approach to identify antecrystic zircons. Earth-Sci. Rev. 176, 87–116.

Smythe, J.D., Brenan, J.M., 2016. Magmatic oxygen fugacity estimated using zircon-melt partitioning of cerium. Earth Planet. Sci. Lett. 453, 260–266.

Sparks, R.S.J., Young, S.R., 2002. The eruption of Soufrière Hills Volcano, Montserrat (1995 to 1999): overview of scientific results. In: Druitt, T.H., Kokelaar, B.P. (Eds.), The Eruption of Soufrière Hills Volcano, Montserrat, from 1995–1999. Geological Society, London, pp. 45–69 Memoir 21.

Stinton, A.J., Cole, P.D., Stewart, R.C., Odbert, H.M., Smith, P., 2014. Chapter 7 The 11 February 2010 partial dome collapse at Soufrière Hills Volcano, Montserrat. In: Wadge, G., Robertson, R.E.A., Voight, B. (Eds.), The Eruption of Soufrière Hills Volcano, Montserrat from 2000 to 2010. Geological Society, London, pp. 133–152 Memoir 39.

Storm, S., Shane, P., Schmitt, A.K., Lindsay, J.M., 2012a. Decoupled crystallization and eruption histories of the rhyolite magmatic system at Tarawera volcano revealed by zircon ages and growth rates. Contrib. Mineral. Petrol. 163, 505–519.

Szymanowski, D., Wotzlaw, J.F., Ellis, B.S., Bachmann, O., Guillong, M., Von Quadt, A., 2017. Protracted near-solidus storage and pre-eruptive rejuvenation of large magma reservoirs. Nat. Geosci. 10, 777–782.

Tollan, P., Hermann, J., 2019. Arc magmas oxidised by water dissociation and hydrogen incorporation in orthopyroxene. Nat. Geosci. 12, 667–671.

Trail, D., Watson, B.E., Tailby, N.D., 2012. Ce and Eu anomalies in zircon as proxies for the oxidation state of magmas. Geochim. Cosmochim. Acta 97, 70–87.

Troch, J., Ellis, B.S., Schmitt, A.K., Bouvier, A.S., Bachmann, O., 2018. The dark side of zircon: textural, age, oxygen isotopic and trace element evidence of fluid saturation in the subvolcanic reservoir of the Island Park-Mount Jackson Rhyolite, Yellowstone (USA). Contrib. Mineral. Petrol. 173, 1–17.

Ubide, T., Kamber, B.S., 2018. Volcanic crystals as time capsules of eruption history. Nat. Commun. 9, 1–12.

Wadge, G., Voight, B., Sparks, R.S.J., Cole, P.D., Loughlin, S.C., Robertson, R.E.A., 2014. An overview of the eruption of Soufrière Hills Volcano, Montserrat from 2000 to 2010. In: Wadge, G., Robertson, R.E.A., Voight, B. (Eds.), The Eruption of Soufrière Hills Volcano, Montserrat from 2000 to 2010. Geological Society, London, pp. 1–40 Memoir 39.

Watson, E.B., 1996. Dissolution, growth and survival of zircons during crustal fusion: kinetic principles, geological models and implications for isotopic inheritance. Geol. Soc. Am. Spec. Pap. 315, 43–56.

Watson, E.B., Harrison, T.M., 1983. Zircon saturation revisited: temperature and composition effects in a variety of crustal magma types. Earth Planet. Sci. Lett. 64, 295–304.

Young, S.R., Sparks, R.S.J., Aspinall, W.P., Lynch, L.L., Miller, A.D., Robertson, R.E.A., Shepherd, J.B., 1998. Overview of the eruption of Soufrière Hills Volcano, Montserrat, 18 July 1995 to December 1997. Geophys. Res. Lett. 25, 3389–3392.

Zellmer, G.F., Hawkesworth, C.J., Sparks, R.S.J., Thomas, L.E., Harford, C.L., Brewer, T.S., Loughlin, S.C., 2003a. Geochemical evolution of the Soufrière Hills Volcano, Montserrat, Lesser Antilles Volcanic Arc. J. Petrol. 44, 1349–1374.

Zellmer, G.F., Sparks, R.S.J., Hawkesworth, C.J., Wiedenbeck, M., 2003b. Magma emplacement and remobilization timescales beneath Montserrat: insights from Sr and Ba zonation in plagioclase phenocrysts. J. Petrol. 44, 1413–1431.